Journal of Materials Chemistry A

ROYAL SOCIETY OF CHEMISTRY

PAPER

View Article Online
View Journal

Cite this: DOI: 10.1039/d6ta01987k

Understanding the catalytic site structure in metal poly(heptazine imide)–crystalline carbon nitride

Dario Calvani, *[ab] Isadora G. Farias,[c] Diandra Nunes Barreto,[c] Luis F. G. Noleto,[c] Marcos A. R. da Silva, [c] Ivo F. Teixeira, *[c] Agnieszka Kuc*[ab] and Thomas D. Kühne[ab]

Metal poly(heptazine imide) (M-PHI), a crystalline carbon nitride, has emerged as a highly promising platform for surface and single-atom catalysis (SAC). However, the precise structure and coordination environment of its catalytically active sites remain unresolved. In this work, we elucidate the structure of a representative M-PHI catalytic site, nickel poly(heptazine imide) (Ni-PHI), through a synergistic experimental–computational approach integrating synthesis, characterization, and CO probe-assisted diffuse reflectance infrared Fourier transform spectroscopy (CO-DRIFTS) with DFT-based static and molecular dynamics simulations combined with vibrational density-of-states analysis of CO bond stretching (CO-VDOS). By systematically assessing different nickel loadings, examining the formation of nickel single atoms and nickel-based nanoparticles, comparing static and dynamic DFT energetics, and correlating the experimentally measured CO-DRIFTS spectra with the simulated CO-VDOS features, we identify highly probable Ni-PHI catalytic site structures that account for nickel single-atom and nickel-based nanoparticle cases. This work provides a general and efficient experimental–computational strategy for molecularly understanding the catalytic sites in metal poly(heptazine imide)–crystalline carbon nitrides.

Received 6th March 2026
Accepted 30th April 2026

DOI: 10.1039/d6ta01987k

rsc.li/materials-a

1 Introduction

Over the past two decades, extensive research has focused on two-dimensional (2D) carbon nitride-based materials (g-C_3N_4) for artificial photosynthesis, aiming at the sustainable production of solar fuels (*e.g.*, H_2 and H_2O_2) and high-energy carbon compounds (*e.g.*, CH_3OH, CO, and CH_4), starting from abundant raw sources such as H_2O, CO_2, and N_2.[1,2] As recently outlined by Pelicano and Antonietti, the structure of the layered polymeric semiconductor g-C_3N_4, usually categorized by its triazine or heptazine units, can also be classified based on its covalent or ionic structure.[3] Both types of carbon nitride have arisen as excellent candidates to achieve efficient single-atom catalysis (SAC), hosting single metal atoms coordinated into the carbon–nitrogen framework.[3] Focusing on heptazine-based carbon nitride structures as highly favorable for holding SAC, the covalent type displays an sp^2-hybridization, with sporadic charge and holes delocalized in the C–N framework, and with the heptazine units connected *via* amine bridges.[3,4] The ionic-type heptazine-based g-C_3N_4 material, also defined as a 2D crystalline ionic carbon nitride, was first reported in 2015 by Dontsova *et al.* with the synthesis of a metal poly(heptazine imide) (M-PHI) based on potassium ions (K-PHI).[5] Specifically, for PHI, the large pores in the C–N framework allow for the accommodation of metal ions coordinated to the negatively charged N atoms on the imide bridges, providing unique photophysical properties, such as time-delayed catalytic function.[6] The accurate investigation of the PHI structure was found to be crucial for correlating the (photo)catalytic performance with specific structural features.[3] While K-PHI's initial models gave heptazine units in an AAA stacking, later studies have reported different interlayer stackings, with potassium atoms positioned nearer to the central region of the channels and between the layers.[7] Pioneered by the work of Savateev *et al.*,[8] further recent research demonstrated that K^+ ions, intercalated in the PHI framework, display mobility, thus allowing for their exchange with other cations among alkali metals, alkaline-earth metals, organic cations, and, of particular catalytic interest, transition metals.[8–17] Initially, noble metals such as platinum played the most prominent role as cocatalysts within PHI for SAC, but at impractical costs due to their low natural abundance.[18] Recently, among the non-noble transition metals,[19,20] nickel has emerged as a highly promising candidate within the PHI framework (Ni-PHI) for sustainable and efficient photo- and electro-SAC applications, including H_2 evolution, H_2O_2 generation, synthesis of organic compounds, and potential CO_2

[a]Helmholtz-Zentrum Dresden-Rossendorf (HZDR), Bautzner Landstrasse 400, 01328 Dresden, Germany. E-mail: d.calvani@hzdr.de; a.kuc@hzdr.de

[b]Center for Advanced Systems Understanding (CASUS), Conrad-Schiedt-Strasse 20, 02826 Görlitz, Germany

[c]Department of Chemistry, Federal University of São Carlos, 13565-905, São Carlos, SP, Brazil. E-mail: ivo@ufscar.br

reduction.[21–26] On the covalent carbon nitride side, Allasia *et al.* reported an elegant first study of the nickel catalytic sites, identifying a melon-type g-C_3N_4 structure as the most favorable for potential SAC.[27] In parallel, recent advancements in ionic carbon nitride research highlight PHI as an efficient, highly versatile, and stable framework for metal-based and, specifically, nickel-based SAC.[12,23] At the beginning of 2026, Guimarães Noleto *et al.* reported a novel example of the Ni-PHI catalytic potential for the photocatalytic hydrogenation of alkynes using water as a hydrogen source, noting a variation in the catalytic turnover frequency (TOF) with Ni content.[26] Similarly, Silva *et al.* demonstrated that Ni-PHI with low Ni loadings display higher TOFs for the selective nitrobenzene coupling into azo/azoxy compounds, also indicating that single-atom species are more active than cluster/nanoparticles.[23] This calls for an urgent and accurate understanding of the M-PHI catalytic site structure and its local coordination environment.

In this study, we present a general integrated experimental and computational strategy to investigate the catalytic site structure in M-PHI, focusing on the Ni-PHI case. We monitored the CO molecular probing of the nickel catalytic sites both experimentally and theoretically using spectroscopic probe-assisted techniques combined with multiscale computational approaches. Crystalline Ni-PHI with varying nickel concentrations was experimentally synthesized and characterized using X-ray diffraction (XRD), high-angle annular dark-field scanning transmission electron microscopy (HAADF-STEM), elemental mapping using energy dispersive X-ray spectroscopy (EDS), and X-ray photoelectron spectroscopy (XPS). Following CO adsorption probing, the CO frequencies at the catalytic sites were evaluated *via* diffuse reflectance infrared Fourier transform spectroscopy (CO-DRIFTS) for the different nickel loadings. Density functional theory (DFT)-based static calculations were employed to gain energetic, electronic, and conformational insights into the Ni-PHI catalytic site structure. We performed DFT-based *ab initio* molecular dynamics (DFT-MD) simulations to investigate the dynamics of Ni-PHI at room temperature and the vibrational modes of the CO molecular probe, with correlated CO frequencies analyzed across different Ni-PHI configurations. By combining experimental characterization and spectroscopic analysis with DFT-based static and DFT-MD simulations, we identified the formation of either a linear Ni–CO σ-bond or a π-backdonation Ni–CO–Ni bridge interaction depending on the nickel amount and localization, as well as the formation of nickel-based nanoparticles, thus revealing favorable Ni-PHI configurations for the catalytic site. Overall, this study establishes a combined computational–experimental protocol for accurately resolving the M-PHI catalytic site structure and provides insight for the potential rational design of M-PHI toward highly efficient surface and single-atom catalysis.

2 Results and discussion

2.1 Ni-PHI synthesis and characterization

Experimentally, Ni-PHI was prepared following the protocol reported in the work by da Silva *et al.*, as detailed in the Experimental methods section.[23] Successively, the Na-PHI and the Ni-PHI systems with increasing nickel loadings (0.5–4 wt%) were characterized by XRD patterns, as shown in Fig. 1a. The reflections at 8.3° and 14.2° are indicative of the 2D ordering of heptazine units, while the peaks at 25° and 29° correspond to interlayer stacking, which diminishes with increasing nickel concentration. This change in intensity is also in line with the XRD patterns estimated from the DFT simulations (Fig. S1 and the DFT-based static simulations section). This reduction in crystallinity is attributed to nickel coordination (cation exchange), which alters the diffraction pattern through electrostatic interactions and loss of hydration water from the sodium coordination shell.[23,28] High-angle annular dark-field scanning transmission electron microscopy (HAADF-STEM) images further reveal the nickel distribution. For the low-loading sample (0.5 wt%, Fig. 1b), only atomically dispersed Ni species are observed as bright spots, which are highlighted by circles in the image. In contrast, the higher-loading sample (4 wt%, Fig. 1c) shows both isolated single atoms and predominantly nickel-based clusters and nanoparticles, indicating aggregation at elevated nickel concentrations (highlighted by circles). The lattice distances of these nanoparticles were measured to be 0.245 nm and 0.205 nm, attributed to the (111) and (200) planes of NiO, respectively, as shown in Fig. 1d.[29,30] Furthermore, a region predominantly containing nanoparticles was selected (Fig. 1e), and the particle sizes displayed a median of 1.97 nm, as calculated from the particle size distribution histogram in Fig. 1f.

To evaluate the elemental distribution and confirm the successful incorporation of nickel, EDS mapping was performed on the Ni-PHI 0.5 wt% sample. Fig. 2 shows an HAADF-STEM image and corresponding EDS elemental mapping, illustrating the spatial distribution of nitrogen (N) and nickel (Ni). The EDS spectrum of the Na-PHI sample is shown in Fig. S2. The uniform dispersion of both elements throughout the sample indicates the successful incorporation of nickel into the PHI framework and suggests good interaction between the metal species and the support. The quantification of nickel loading was performed by Inductively Coupled Plasma Optical Emission Spectroscopy (ICP-OES) and is reported in Table S1.

To further clarify the chemical composition and oxidation state of surface elements in Ni-PHI materials, X-ray photoelectron spectroscopy (XPS) analyses were performed. High-resolution spectra in the N 1s region, reported in Fig. 3a, show the presence of four typical signals after peak fitting, which can be assigned to pyridinic nitrogen (398.7 eV), amino groups (399.9 eV), graphitic nitrogen (401.2 eV), and π–π^* interactions (404.2 eV). This spectral pattern remains unchanged with varying nickel loadings, indicating that increasing Ni loading does not significantly affect the nitrogen chemical environment of the PHI framework. In the O 1s XPS region, an important trend can be observed as a function of nickel loading (Fig. 3b). With increasing Ni content, the intensity of the signal associated with hydroxyl species increases accordingly. More importantly, a clear change in the peak profile and a systematic shift in binding energy are observed when comparing Ni-PHI 0.5 wt% with Ni-PHI 1 wt%, 2 wt%, and 4 wt%. This behavior indicates the presence of distinct hydroxyl

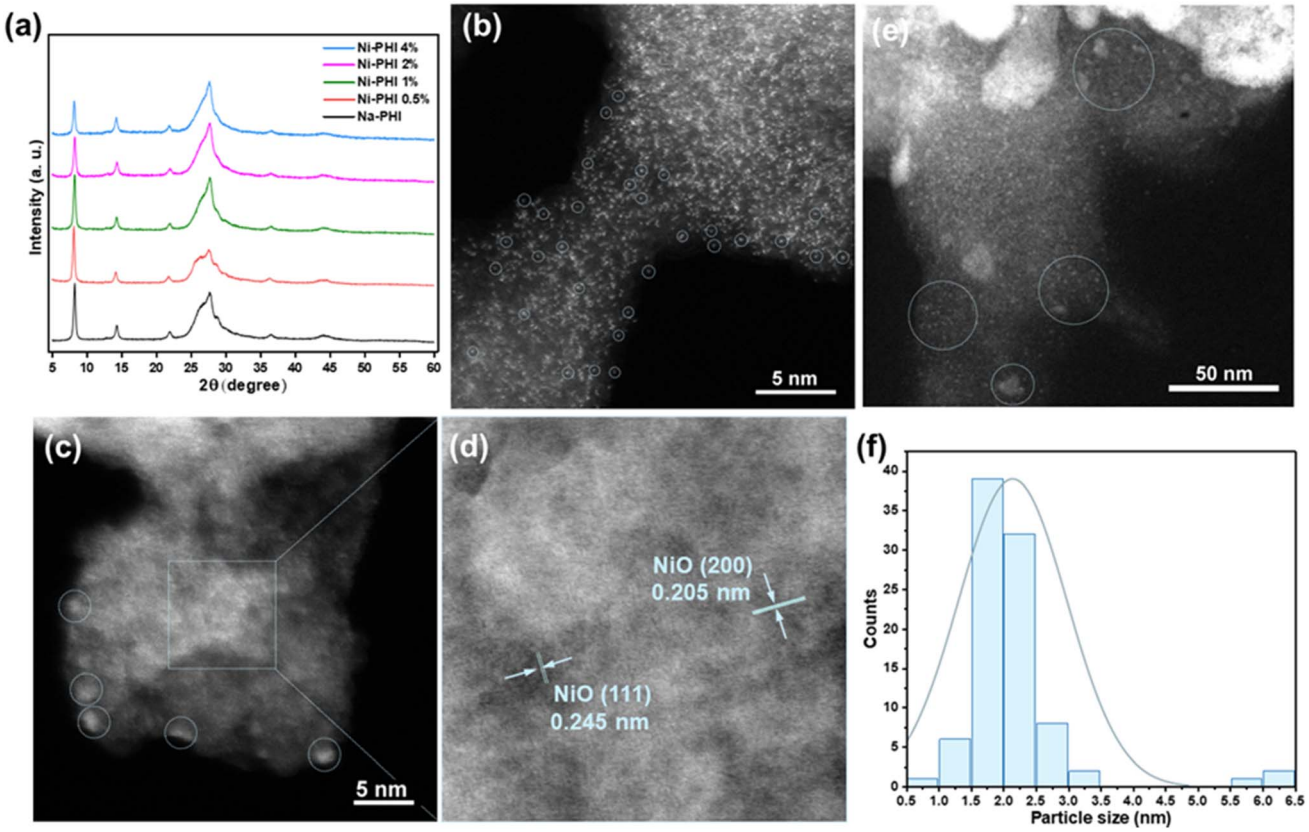

Fig. 1 (a) X-ray diffraction (XRD) of Na-PHI and Ni-PHI with different nickel loadings (0.5 wt%, 1 wt%, 2 wt%, 3 wt%, and 4 wt%). (b) HAADF-STEM image of Ni-PHI (0.5 wt%) showing atomically dispersed Ni species. (c) HAADF-STEM image of Ni-PHI (4 wt%) showing Ni-based clusters and nanoparticles, likely such as NiO and/or $Ni(OH)_2$. (d) Lattice fringes corresponding to the (111) and (200) planes of NiO. (e and f), Representative region containing clusters and nanoparticles, and the particle size distribution diagram for Ni-PHI (4 wt%).

environments among the samples. The progressive increase of the OH-related signal with higher metal loading strongly suggests the formation of $Ni(OH)_2$ species within the PHI surface. This assignment is supported by the emergence of a component around 531.2 eV, which is characteristic of nickel hydroxide.[31,32] In contrast, for Ni-PHI 0.5 wt%, the OH-related contribution appears at a higher binding energy (531.8 eV), which is more consistent with surface-adsorbed hydroxyl species and/or C–O functionalities.[33–35] Overall, these results indicate that the incorporation of higher amounts of nickel into the PHI structure promotes the formation of nickel hydroxide species at the surface. The remaining components in the O 1s region can be attributed to adsorbed water (533.0 eV) and to the Na KLL Auger signal arising from sodium cations present in the PHI structure.

In the Ni 2p XPS region, no significant differences are observed among the samples (Fig. 3c), indicating that the overall oxidation state of nickel does not vary with metal loading. The main Ni $2p_{3/2}$ peak is located at 855.8 eV, which is consistent with the presence of Ni^{2+} species in all samples. For the Ni-PHI 4 wt% sample, we attempted to fit the Ni 2p spectrum using the $Ni(OH)_2$ reference parameters reported by Biesinger *et al.*[31] However, a noticeable mismatch in the fitting was observed (Fig. S3). This discrepancy suggests that the nickel species in Ni-PHI are not exclusively present as $Ni(OH)_2$. A reliable peak fitting is difficult to achieve since we probably have a mixture of isolated nickel sites and clusters of nickel hydroxide in the Ni-PHI 4 wt% sample.

2.2 CO adsorption probing *via* diffuse reflectance infrared Fourier transform spectroscopy (CO-DRIFTS)

The CO-DRIFTS spectroscopy analysis was performed on Ni-PHI samples for each Ni concentration (0.5 wt%, 1 wt%, 2 wt%, and 4 wt%). The samples were pretreated at 300 °C and analyzed as detailed in the Experimental methods section. In Fig. 4, we report the CO-DRIFTS spectra of Ni-PHI materials. For the Ni-PHI 0.5 wt% and 1 wt% samples, bands at 2188 and 2190 cm^{-1}, respectively, are assigned to linearly σ-bonded chemisorbed CO on Ni^{2+} sites, while the band at 2135 cm^{-1} corresponds to physiosorbed CO, reflecting weak and reversible interactions with the surface.[27,36,37] At nickel concentrations of 2 wt% and above, the CO bands red-shift to lower frequencies than the 0.5–1 wt% cases, consistent with the possible presence of π-backdonation and decreased polarization of the CO molecule. The bands observed at 2075–2080 cm^{-1} and 2006 cm^{-1} in the Ni-PHI 2 wt% and 4 wt% samples are likely associated with bridge-bonded CO (Ni–CO–Ni), indicating the presence of sites where the molecule is simultaneously coordinated to two metal atoms.[38,39] In this concentration range, the intensity of bands associated with linear CO adsorption

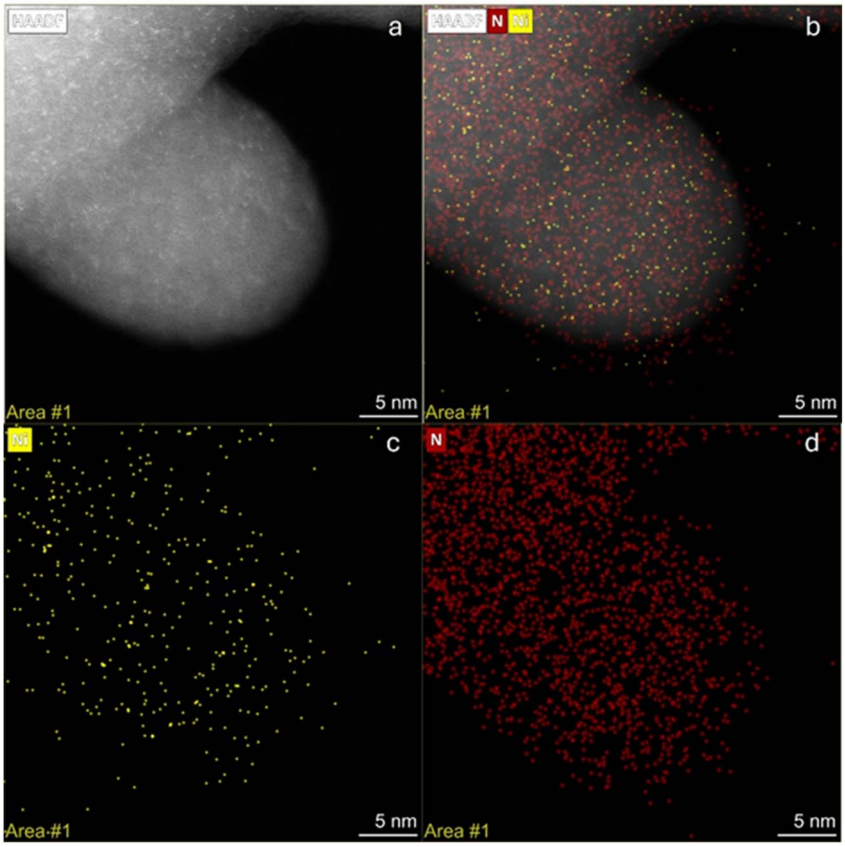

Fig. 2 Elemental analysis of the Ni-PHI 0.5 wt% sample. (a) HAADF-STEM image; (b) EDS elemental mapping showing the distribution of Ni and N; (c) mapping of Ni; (d) mapping of N.

decreases significantly, suggesting the formation of nickel clusters or nanoparticles, most likely composed of $Ni(OH)_2$, and/or NiO species, since the samples are pretreated at 300 °C and the hydroxyl groups might dissociate.[40–42] The predominance of bridge-bonded CO bands reinforces this hypothesis. To investigate the possible formation of NiO particles after the thermal treatment performed prior to the CO-DRIFTS analysis, XPS measurements were carried out on the

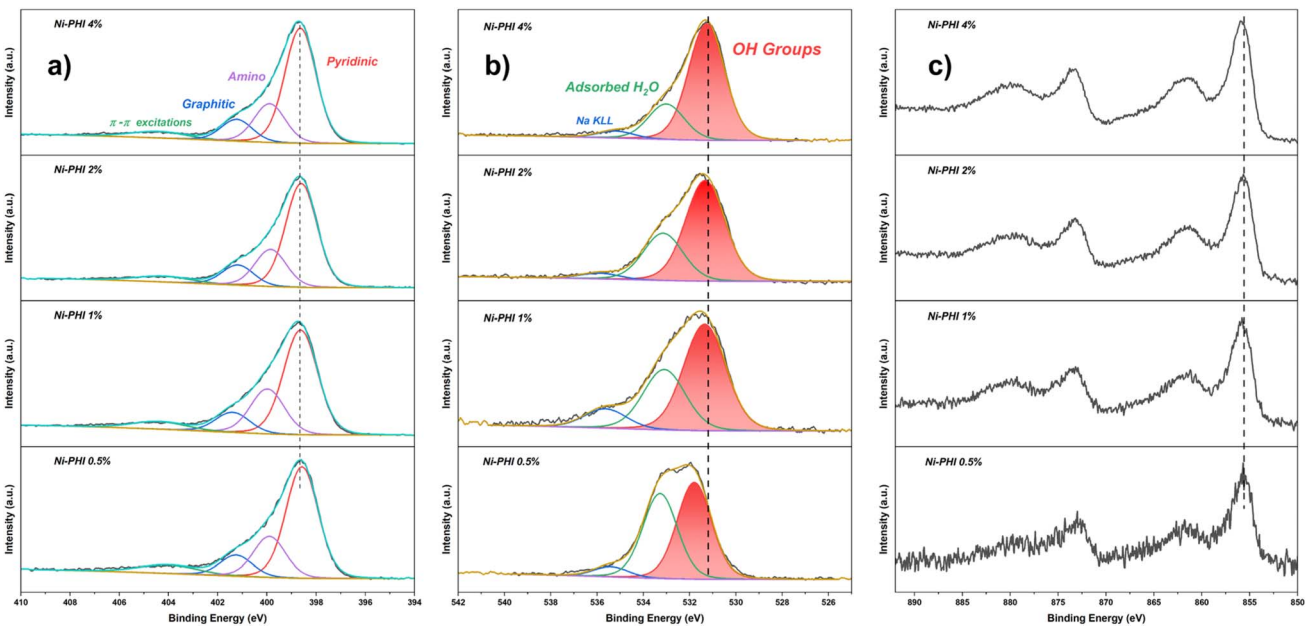

Fig. 3 High-resolution XPS (a) N 1s, (b) O 1s, and (c) Ni 2p spectra of Ni-PHI 4 wt%, 2 wt%, 1 wt% and 0.5 wt%.

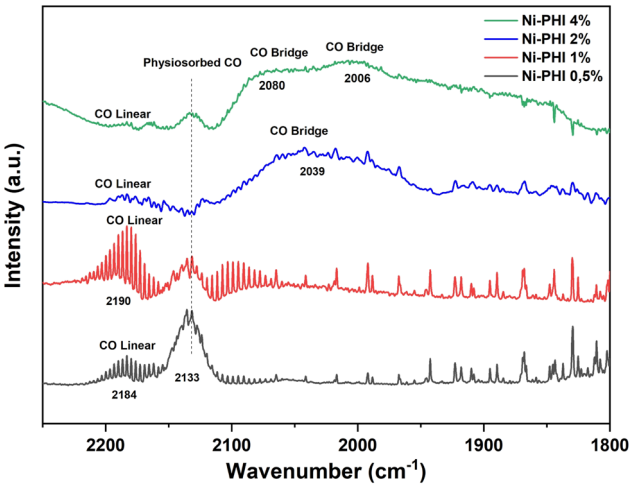

Fig. 4 Kubelka–Munk plots of CO desorption from Ni-PHI measured by CO-DRIFTS. Intensities are in arbitrary units (a.u.) and frequencies are in cm^{-1}. Ni-PHI samples with 0.5 wt%, 1 wt%, 2 wt%, and 4 wt% nickel concentration are shown in black, red, blue, and green, respectively.

Ni-PHI 4% sample after treatment (Fig. S4 and S5). The high-resolution O 1s spectrum can be fitted into four components. The peak at higher binding energy is attributed to the Na KLL Auger feature, while the contributions at 533.0 eV and 531.5 eV are assigned to adsorbed water and hydroxyl groups, respectively, consistent with the observations for the untreated sample. Notably, a new feature emerges at lower binding energy (530.4 eV), which is characteristic of NiO and confirms the formation of NiO clusters upon thermal treatment.[43,44] In contrast, the high-resolution Ni 2p region does not show significant changes and does not resemble the profile of NiO.[31] This suggests the coexistence of different Ni species in the material, including isolated Ni single atoms and NiO clusters.

Considering that the CO-DRIFTS peak intensity is proportional to the available metal surface area, the results indicate that higher nickel concentrations promote the formation of aggregated metallic structures such as $Ni(OH)_2$ and/or NiO nanoparticles, which favor bridge CO adsorption due to the presence of multiple adjacent metal centers. To comprehensively understand the structure of the catalytic sites in Ni-PHI, and correlate the experimental analysis to a molecular description, we performed DFT static and DFT-MD simulations on an extensive series of possible Ni-PHI models and a representative NiO-PHI one. The theoretical models used in the present study are grounded in realistic coordination environments based on X-ray absorption fine structure (XAFS) analysis of da Silva *et al.* and recent studies of Guimarães Noleto *et al.*[20,26]

2.3 DFT-based static simulations: one Ni^{2+} ion within PHI layers (Ni-2(PHI)) and with the adsorbed carbon monoxide molecular probe ((Ni-CO)-2(PHI))

Initially, we investigated the optimal configuration of one Ni^{2+} ion in a double-layer PHI (Ni-2(PHI)), considering both in-plane and out-of-plane starting arrangements, as represented in Fig. 5a and b, respectively (see the Computational methods section for details). To study these systems in a periodic 2D computational fashion and thus achieve a comprehensive description of the nickel ion(s) embedded within a multilayer PHI catalytic site,[13,14,20] we provided for the entire system a total net charge equal to zero by removing two of the six Na^+ ions from an ideal Na-saturated PHI active site, thus depicting a local cation exchange with Ni^{2+} (Fig. 5, orange triangle areas, and Fig. S6).[23] We performed DFT-based static simulations using both DFT and DFT + *U* (Hubbard correction) methods at the GGA level throughout this work to investigate the systems and also obtain a comparison between standard and Hubbard corrected DFT methods (see the Computational methods section for details). The DFT + *U* method served as our primary approach because it is cost-effective and highly reliable at the GGA level for transition-metal complexes in SAC.[45,46] We performed geometry optimizations of the initial structures shown in Fig. 5.

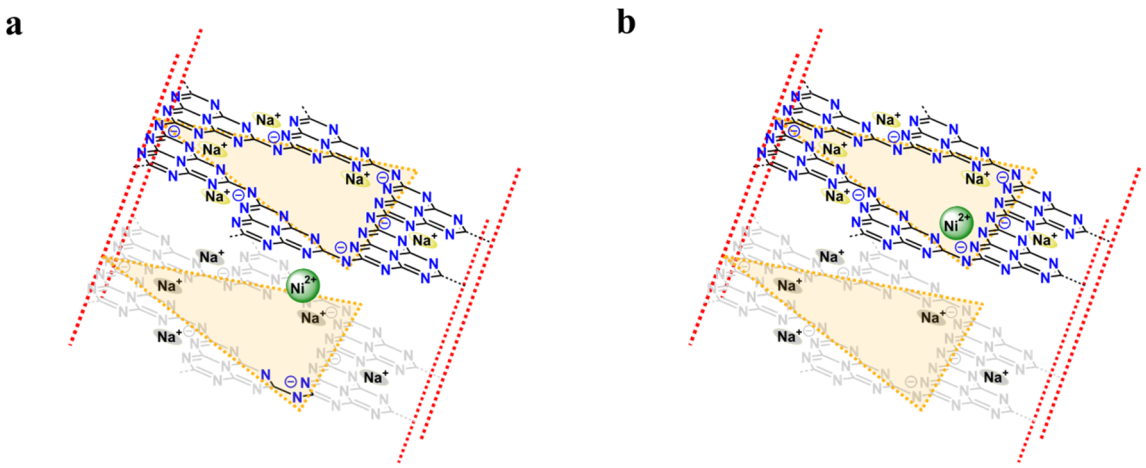

Fig. 5 Idealized 2PHI layers with starting configurations (a) out-of-plane, and (b) in-plane, Ni^{2+} ion: Ni-2(PHI). The orange area describes the catalytically active site with the Ni^{2+} ion. The atoms are sketched in a ball-and-stick representation, with nickel in green, carbon in black, nitrogen in blue, and sodium in yellow. In color and grey, the upper and bottom, respectively, are PHI layers and sodium cations. The interacting part of the bottom PHI layer with the Ni^{2+} ion is kept colored.

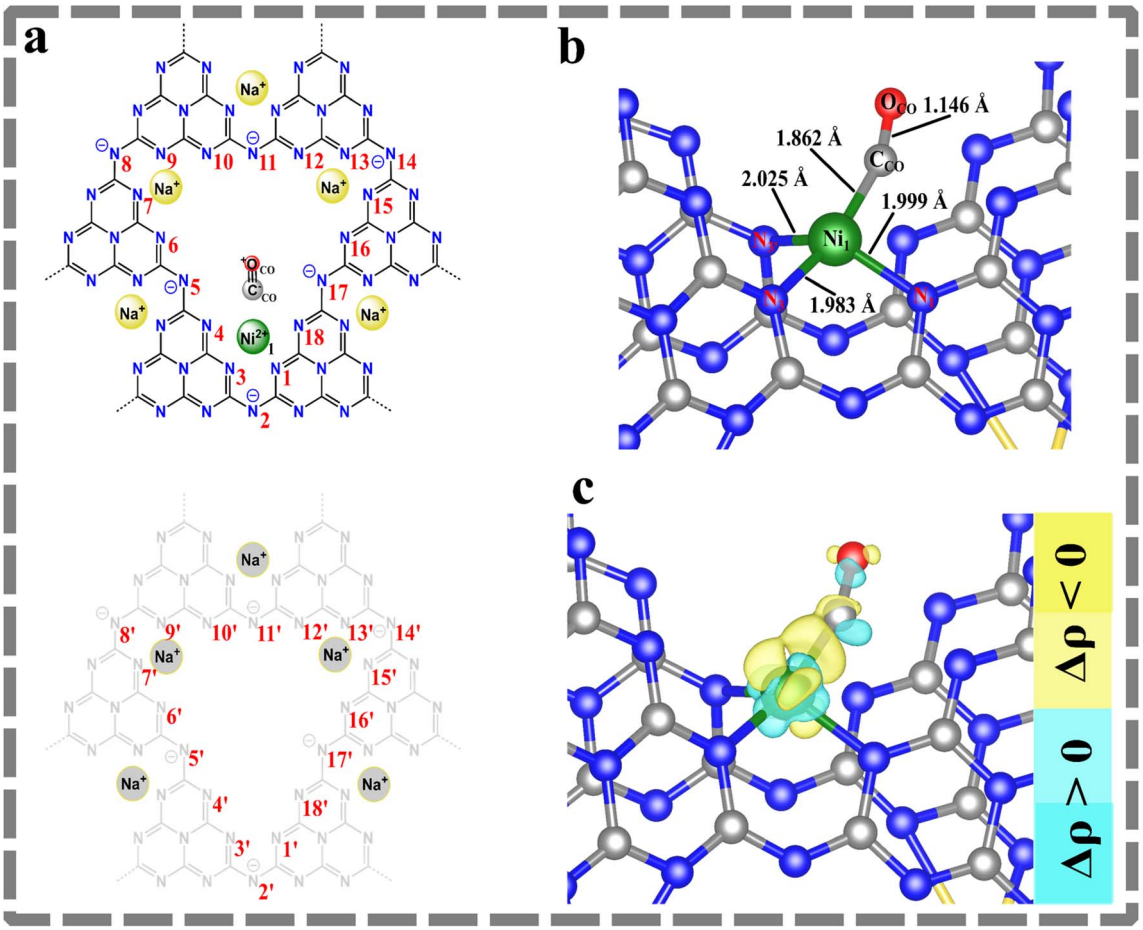

Fig. 6 (a) Idealized (Ni-CO)-2(PHI) with numbering of the Ni^{2+} ion (Ni_1), and CO atoms (C_{CO} and O_{CO}) in black, and N_n atoms ($1 \geq n \geq 18$) in red, without and with the single quote symbol (') for the top and the bottom PHI layers, respectively. The atoms are shown in a ball-and-stick representation, with nickel in green, carbon in black, nitrogen in blue, oxygen in red, and sodium in yellow. In color and grey, the upper and bottom, respectively, are PHI layers and sodium cations. (b) Zoom on the DFT + U geometry optimized (Ni-CO)-2(PHI) system to highlight the Ni_1–C_{CO}, C_{CO}–O_{CO}, and Ni–N_1 (Ni_1–N_1, Ni_1–N_3, and Ni_1–$N_{3'}$) distances. (c) DFT + U charge density difference ($\Delta\rho$) for the (Ni-CO)-2(PHI) system. Yellow and cyan colors are used to represent the negative and positive charge density differences, respectively, with an isosurface value of 0.01. The atoms are depicted as ball-and-stick models, with nickel in green, carbon in grey, nitrogen in blue, oxygen in red, and sodium in yellow.

In both relaxed structures, the Ni^{2+} ion adopts an out-of-plane configuration, with a negligible total energy difference of 0.013 eV between them with respect to thermal energy ($k_B T_{300K} \approx 0.027$ eV). The Ni^{2+} ion coordinates to three nitrogen atoms of the PHI layers with Ni–N distances within the range of $\approx$ 1.9–2.1 Å, indicative of strong metal–nitrogen binding (Fig. S7), and with a triplet electronic state for both DFT + U and DFT approaches.[27,45–47]

Successively, on the energetically most stable optimized configuration, a CO molecule was added in the proximity of the Ni^{2+} ion at a distance of $d(\text{Ni–C}_{CO}) \approx 2$ Å in two different starting positions (see Fig. S8 and the Computational methods section). As also reported in the CO-DRIFTS section, the use of the CO probe molecule is experimentally justified since it is sensitive to the oxidation state and location of metal sites.[27] We optimized the geometry of the (Ni-CO)-2(PHI) system and identified a singlet electronic state for both DFT + U and DFT approaches. We estimated the Ni–CO binding energy (ΔE_B) to be approximately 1.05 eV (1.76 eV for DFT), as detailed in the Computational methods section. We explored the structural configurations to assess the potential π-backdonation (also named π-backbonding) from Ni to CO, such as $Ni^{2+} \rightarrow -C{\equiv}O^+$, outlining the Ni_1–N_n, Ni_1–C_{CO}, and C_{CO}–O_{CO} distances depicted in Fig. 6a and b, S9 a), and the charge density difference (Fig. 6c and S9 b).[48] After CO adsorption, we found the nickel ion still coordinating with three nitrogens in the PHI catalytic site with an average Ni_1–N_n bond length of 2.002 Å (1.955 Å for DFT) within the strong metal–nitrogen interaction range of $\approx$ 1.9–2.0 Å.[27,45,46] According to the classical concept of π-backdonation, the C≡O bond length ($d(C_{CO}–O_{CO})$) of the isolated free CO molecule increases upon interaction with the Ni^{2+} ion. The free CO bond length, $d(C_{free–CO}–O_{free–CO})$, is experimentally estimated to be $d(C_{free–CO}–O_{free–CO})_{exp} = 1.128$ Å (*via* X-ray crystallography).[49] However, in DFT simulations, $d(C_{CO}–O_{CO})$ can vary depending on the level of theory employed, which also shifts the reference value for the free CO bond length. In this work, we used a reference value of $d(C_{free–CO}–O_{free–CO})_{DFT} = 1.144$ Å, obtained from the same level of DFT applied throughout all static

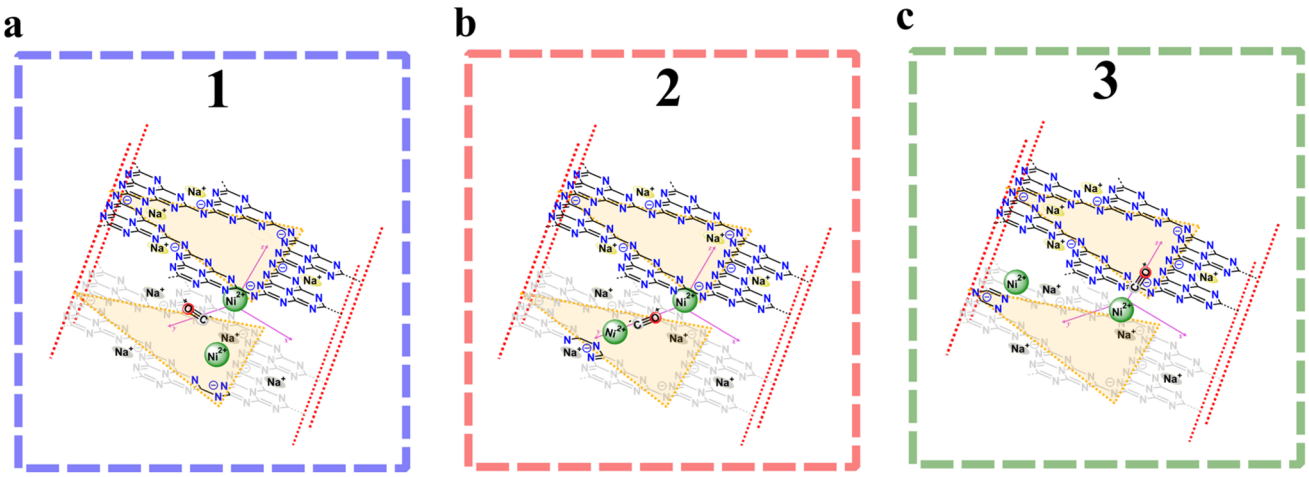

Fig. 7 DFT + *U* case: representative initial idealized three configurations of two out-of-plane Ni^{2+} ions within 2PHI layers with the adsorbed carbon monoxide molecular probe, (Ni_2-CO)-2(PHI): (a) (system **1**), (b) (system **2**), and (c) (system **3**). The orange area describes the catalytically active site with Ni^{2+} ions. The atoms are depicted as ball-and-stick models, with nickel in green, carbon in black, nitrogen in blue, oxygen in red, and sodium in yellow. In color and grey, the upper and bottom, respectively, are PHI layers and sodium cations. The interacting part of the bottom PHI layer with the Ni^{2+} ion is kept colored. The reference *x*, *y*, and *z* axes to mark the initial CO orientation are shown in pink.

DFT calculations (see the Computational methods section), and consistent with previous literature.[50] For the (Ni-CO)-2(PHI) system, $d(C_{CO}–O_{CO})$ shows only a slight elongation to 1.146 Å (1.151 Å for DFT), as reported in Fig. 6b and S9a, indicating no significant π-backdonation interaction between nickel and CO.[48,51] The charge density difference reported in Fig. 6c and S9b reveals localized negative and positive isosurfaces on the oxygen atom of the CO molecular probe, suggesting a slightly less polarized CO bond, compared to the fully polarized isolated CO case.[48] We performed Bader charge analysis on the optimized structures to specifically verify whether nickel retains a positive charge within the periodic framework, as shown in Table S2.[52] In both cases, Ni-2(PHI) and (Ni-CO)-2(PHI), the Bader charge on nickel was found to be positive, +1.11 $|e|$ and +0.96 $|e|$, respectively. Finally, to further ensure an accurate description of the nickel ion within this periodic scheme, we performed geometry optimizations, followed by frequency and Bader charge analyses on the molecular complexes $[Ni-(melem)_2]^{2+}$ and $[(Ni-CO)-(melem)_2]^{2+}$ in both singlet and triplet states, and the free isolated CO molecule (see Fig. S10, Table S3, and the Computational methods section). The obtained spin-state energetic trend was consistent with the periodic calculations, with the $[Ni-(melem)_2]^{2+}$ and $[(Ni-CO)-(melem)_2]^{2+}$ complexes preferably in triplet and singlet spin states, respectively. The trend of the Bader charges on nickel was also in line with the periodic systems, showing values of +1.32 $|e|$ for the $[Ni-(melem)_2]^{2+}$ triplet state complex and +1.11 $|e|$ for the $[(Ni-CO)-(melem)_2]^{2+}$ singlet state complex.

2.4 DFT-based static simulations: two out-of-plane Ni^{2+} ions within PHI layers (Ni_2-2(PHI)) and with the adsorbed carbon monoxide molecular probe ((Ni_2-CO)-2(PHI))

To preliminarily understand the increase in the number of Ni^{2+} ions in the active pocket of the PHI layer, we investigated systems with two nickel ions, such as Ni_2-2(PHI). The total net charge of the entire system in our periodic 2D computational model was set to zero by removing four of the six Na^+ ions from an ideal Na-saturated PHI active site, thus describing a local cation exchange with two Ni^{2+} ions (Fig. S11, orange triangle areas). The initial configurations of the two Ni^{2+} ions are taken out-of-plane, as this was found to be the most stable arrangement for a single Ni^{2+} ion. To explore different nickel positions within the catalytic pocket, we performed geometry optimizations on three system types, varying the position of one Ni^{2+} ion relative to the other within the catalytic pocket. The two Na^+ ions in the catalytic site were considered in two possible swapped arrangements, resulting in a total of six configurations (Fig. S11). For each of the two permutations of Na^+ corresponding to the same Ni^{2+} ion positions in the catalytic pocket, we identified the most stable configurations. For both DFT and DFT + *U* methods, the Ni_2-2(PHI) optimized structures display the Ni^{2+} ions in a sandwich out-of-plane configuration between two PHI layers (Fig. S12). Of these three optimized structures, two adopt configurations in which both Ni^{2+} ions are tri- and tetra-coordinated to the nitrogen atoms of the PHI's catalytic pocket (Fig. S12c–f). In contrast, in one configuration where the two Ni^{2+} ions are constrained to mirror each other within a limited volume, each nickel interacts with the catalytic pocket *via* only Ni–N di-coordination (Fig. S12a and b). The reduced Ni–N coordination for the Ni^{2+} ion mirror system (Fig. S12a and b) may explain why the di-coordinated system is less stable in total energy by ≈1–2 eV compared to the other two configurations shown in Fig. S12c–f. For these three most stable Ni_2-2(PHI) optimized structures, a CO molecule was placed near each nickel atom at $d(Ni_n–C_{CO}) \approx 2$ Å, in two different initial positions, as described for the single Ni^{2+} case in Fig, S8, for a total of twelve initial configurations (four for each system). This setup allows evaluation of the Ni–CO interaction and possible π-backdonation ($Ni^{2+} \rightarrow -C{\equiv}O^+$). After geometry optimization, we identified the three most stable geometries for each of the

Table 1 DFT + U (PBE-D3+U) results: binding energy (ΔE_B) in eV of Ni–CO interaction, and distances (d) in Å for the systems (Ni_2-CO)-2(PHI), **1**, **2**, and **3**. Distances include $\langle Ni_{1,2}–N_n\rangle$ (averaged value), $Ni_{1,2}–C_{CO}$, and $C_{CO}–O_{CO}$, where the N_n atoms ($1 \geq n \geq 18$), without and with the single quote symbol (') correspond to the top and the bottom PHI layers (Fig. 5a), respectively. The binding energy is calculated as $\Delta E_B = E_{(Ni2\text{-}CO)\text{-}2(PHI)} - E_{Ni2-2(PHI)} - E_{CO}$, using single-point calculations on (Ni_2-CO)-2(PHI), and its components Ni_2-2(PHI) and CO, respectively

System	ΔE_B (eV)	$\langle d(Ni_n–N_n)\rangle$ (Å)	$d(Ni_n–C_{CO})$ (Å)	$d(C_{CO}–O_{CO})$ (Å)
(Ni_2-CO)-2(PHI) system **1**	−2.25	1.965 (Ni_1) 1.917 (Ni_2)	1.852 (Ni_1) 2.366 (Ni_2)	1.154
(Ni_2-CO)-2(PHI) system **2**	−1.19	2.261 (Ni_1) 2.075 (Ni_2)	1.934 (Ni_1)	1.140
(Ni_2-CO)-2(PHI) system **3**	−1.50	2.006 (Ni_1) 2.075 (Ni_2)	1.1964 (Ni_1)	1.143

three Ni^{2+} arrangements in the catalytic pocket, labeled **1**, **2**, and **3** (Fig. 7, S13, and S14).

The CO strongly binds to the Ni^{2+} species, with the Ni–CO binding energies (ΔE_B) reported in Table 1 (see the Computational methods for details). For (Ni_2-CO)-2(PHI) system **1**, the binding energy increases by approximately 1.06 eV and 0.75 eV (0.45 eV and 0.10 eV for standard DFT, respectively, Table S4) compared to systems **2** and **3**, respectively. The configuration with the two nickel ions mirrored along the z-axis exhibits the strongest Ni–CO binding among those analyzed.

The structural configurations and charge density difference distributions were then analyzed. The results show that the optimized CO adopts a tilted orientation relative to its initial Ni–CO interacting position (Fig. 8, S14 and S15). The highest binding energy observed for system **1** can be attributed to the catalytic site structure and Ni–N di-coordination, which may enhance the interaction with the CO probe. From the optimized geometries, we outline the $Ni_{1,2}–C_{CO}$, $C_{CO}–O_{CO}$, and $Ni_{1,2}–N_n$ distances (Fig. 8a, c, and e, S15 a, c, and e). The averages of $Ni_{1,2}–N_n$ bond lengths reported in Table 1 (Table S4) indicate strong metal–nitrogen interactions ($\approx$1.9–2.0 Å) for system 1, and mild ($\approx$2.1–2.2 Å) metal–nitrogen interactions for systems **2** and **3**.[27,45,46] Notably, in (Ni_2-CO)-2(PHI) system **1**, the two mirrored Ni^{2+} ions are both within interacting distance of the CO molecular probe, $Ni_1–C_{CO}$ and $Ni_2–C_{CO}$, respectively (Table 1 and Table S4). This configuration can be described as a semi-bridge Ni–CO–Ni interaction, due to an asymmetry in the Ni–C_{CO} bond lengths of 1.852 Å and 2.366 Å (Table 1 and Table S4), respectively. This particular semi-bridge interaction likely accounts for the stronger Ni–CO binding energy, compared to the linear Ni–CO interaction in systems **2** and **3**, as reported in Table 1 (Table S4). As a consequence of this strong Ni–CO binding, the $C_{CO}–O_{CO}$ bond length increases to 1.154 Å (Table 1 and Table S4) in system **1**, compared to the free isolated CO molecule ($d(C_{free-CO}–O_{free-CO})_{DFT}$ = 1.144 Å) and systems **2** (1.140 Å) and **3** (1.143 Å), as detailed in Table 1 (Table S4). This elongation indicates an enhanced metal–CO interaction due to a $Ni^{2+} \rightarrow -C{\equiv}O^+$ π-backdonation in system **1**.[48,51] On the other hand, for systems **2** and **3**, the CO bond length is shorter than that of the isolated CO molecule, suggesting the formation of a linear Ni–CO σ-bond accompanied by a decrease in the electron density of the weakly antibonding 5σ orbital of CO or electrostatically physiosorbed CO, thus resulting in a shorter CO bond than free CO. Furthermore, the charge density difference analysis shown in Fig. 8 and S15 reveals a more localized negative isosurface on both the C_{CO} and O_{CO} atoms in system **1** than in systems **2** and **3**, suggesting a less polarized CO molecule (C=O) for the former, whereas the latter systems exhibit a persistently polarized CO ($^-C{\equiv}O^+$). This is consistent with a longer CO bond in system **1** than in systems **2** and **3**. We performed Bader charge analysis on the Ni_2-2(PHI) and corresponding (Ni_2-CO)-2(PHI) optimized structures to verify whether nickel preserves a positive charge within the periodic framework.[52] As reported in Table S2, the Bader charges on nickel atoms were found to be positive in all cases, supporting the reliability of our periodic approach. Interestingly, a higher positive charge was observed for both the nickel atoms in (Ni_2-CO)-2(PHI) system **1** compared to the ones in (Ni_2)-2(PHI) system **1**, indicating $Ni^{2+} \rightarrow -C{\equiv}O^+$ π-backdonation upon CO interaction. Conversely, for the other systems, the presence of CO leads to a decrease in the positive charge on the nickel bound to CO (Table S2), consistent with a predominantly linear σ-type interaction between Ni^{2+} and CO. Moreover, in (Ni_2-CO)-2(PHI) system **1**, the sum of the Bader charges on the CO probe molecule results in a negative value compared to (Ni-CO)-2(PHI) system and (Ni_2-CO)-2(PHI) systems **2** and **3**, where the sums remain positive (Table S2), further evidencing π-backdonation only in system **1**. Overall, these findings indicate a Ni–CO π-backdonation in (Ni_2-CO)-2(PHI) system **1**, in line with the higher binding energy ΔE_B compared to systems **2** and **3**, where Ni interacts linearly with CO or electrostatically *via* physisorption.

Notably, at the standard DFT level, the calculated spin states among the three (Ni_2-CO)-2(PHI) systems are different: quintet for system **1**, and triplet for systems **2** and **3**. This discrepancy can arise because standard DFT tends to over-delocalize the nickel 3d electrons. As a result, Ni^{2+} ions in different positions may artificially stabilize different spin states due to varying degrees of hybridization with the surrounding carbon nitride framework. In contrast, the DFT + U calculations yield a quintet spin state for these three systems. The Hubbard correction localizes the nickel 3d electrons more effectively, enforcing a more consistent d^8 electronic configuration across all nickel sites. The DFT + U approach leads to a uniform high-spin state and provides a more reliable and physically consistent description of the nickel electronic structure in the PHI catalytic

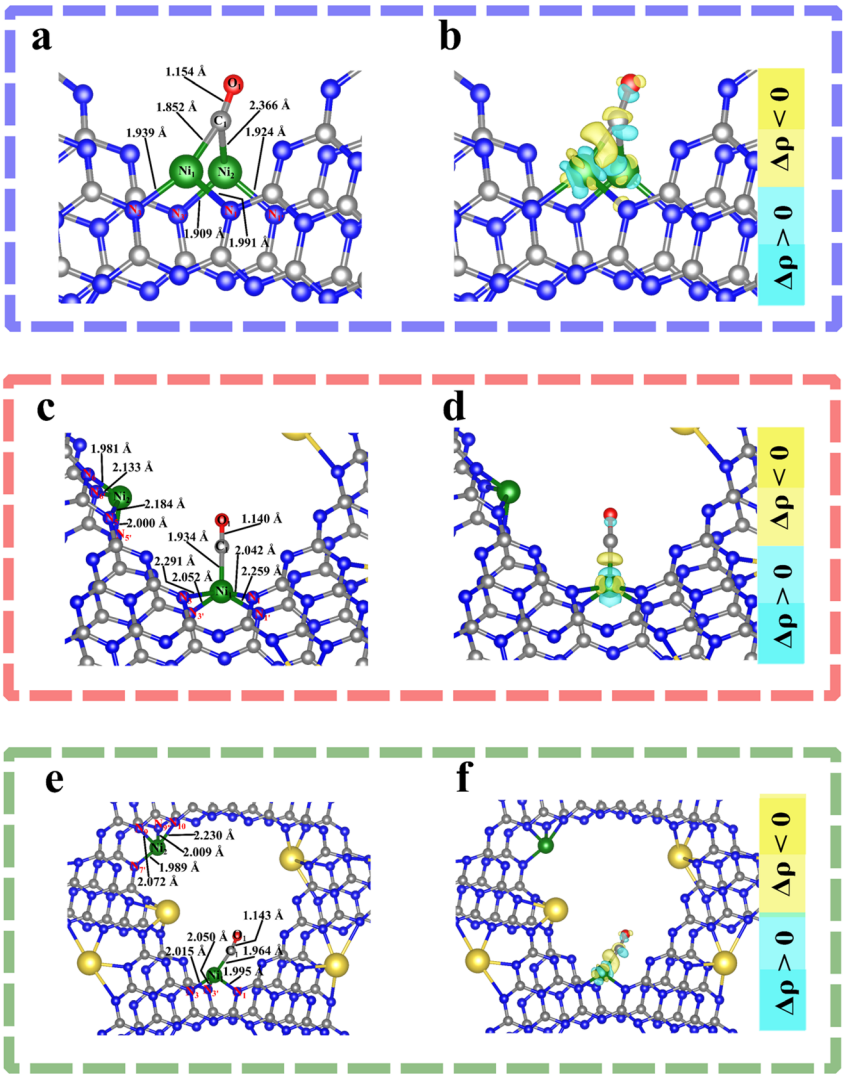

Fig. 8 DFT + *U* geometry-optimized three configurations of two out-of-plane Ni^{2+} ions within 2PHI layers with an adsorbed carbon monoxide molecular probe, (Ni_2-CO)-2(PHI): (a) (system **1**), (c) (system **2**), and (e) (system **3**), inside the blue, red, and green dashed line boxes, respectively. Highlighted $Ni_{1,2}$–C_{CO}, C_{CO}–O_{CO}, and $Ni_{1,2}$–N_n distances, with N_n atoms ($1 \geq n \geq 18$), without and with the single quote symbol (') for the top and the bottom PHI layers, respectively. DFT + *U* charge density difference ($\Delta\rho$) for the (Ni_2-CO)-2(PHI) system: (b) (system **1**), (d) (system **2**), and (f) (system **3**), inside the blue, red, and green dashed line boxes, respectively. Yellow and cyan colors are used to represent the negative and positive charge density differences, respectively, with an isosurface value of 0.01. The atoms are depicted as ball-and-stick models, with nickel in green, carbon in grey, nitrogen in blue, oxygen in red, and sodium in yellow.

pocket than standard DFT. Di Liberto *et al.* reported that for a single nickel atom tetracoordinated to nitrogens in a pyridinic N-doped graphene-like (Gr) system (Ni(4N–Gr)), the spin polarization was almost unaffected by the Hubbard correction compared to other transition metals.[45] On the other hand, our (Ni_2-CO)-2(PHI) systems, containing two Ni^{2+} ions in the same catalytic pocket at different positions, and in a sandwich configuration between two PHI layers, represent a case where the Hubbard correction to GGA-based DFT features as decisive in ensuring the reliability of the electronic structure description. This behavior may be related to the diverse coordination modes of Ni^{2+} ions toward the periodic multilayer PHI, deviating from the conventional Ni(4N–Gr)-type tetra-coordination interaction.

2.5 DFT-based static simulations: a representative NiO-nanoparticle model with an adsorbed carbon monoxide molecular probe (($Ni_{10}O_8$-CO)-2(PHI))

To understand the effect of the likely presence of a nickel oxide (NiO) nanoparticle within the PHI catalytic system, after the pretreatment at 300 °C as highlighted by the experiments, we generated a representative ($Ni_{10}O_8$)-2(PHI) model. This model was chosen to have a typical cubic NiO crystal structure fitting the PHI pore volume,[53] and providing a site for CO probe interaction. The total net charge of the entire system in our 2D periodic framework was set to zero by removing four of the six Na^+ ions from an ideal Na-saturated PHI active site, thus describing a charged $(Ni_{10}O_8)^{4+}$ cluster (Fig. 9a). The

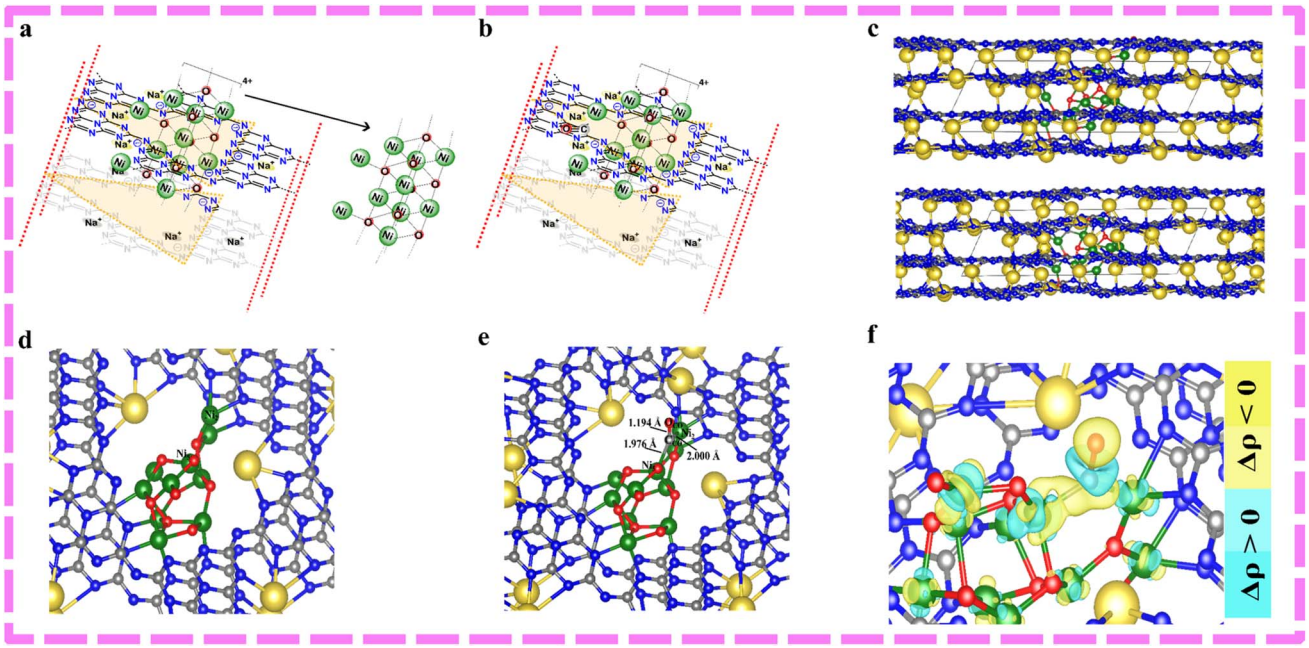

Fig. 9 Representative initial idealized 2PHI layers with (a) a nickel oxide cluster $(Ni_{10}O_8)^{4+}$, $(Ni_{10}O_8)$-2(PHI), and (b) a nickel oxide cluster $(Ni_{10}O_8)^{4+}$ interacting with a carbon monoxide molecular probe, $(Ni_{10}O_8$-CO)-2(PHI). The orange area describes the catalytically active site with a nickel oxide cluster $(Ni_{10}O_8)^{4+}$. The atoms are depicted as ball-and-stick models, with nickel in green, carbon in black, nitrogen in blue, oxygen in red, and sodium in yellow. In color and grey, the upper and bottom, respectively, are PHI layers and sodium cations. The interacting part of the bottom PHI layer with a nickel oxide cluster $(Ni_{10}O_8)^{4+}$ is kept colored. (c) Side views of DFT + U geometry-optimized $(Ni_{10}O_8)$-2(PHI), and $(Ni_{10}O_8$-CO)-2(PHI) systems, top and bottom, respectively. DFT + U geometry-optimized configurations of (d) $(Ni_{10}O_8)$-2(PHI) and (e) $(Ni_{10}O_8$-CO)-2(PHI), respectively. Highlighted $Ni_{2,5}$–C_{CO}, and C_{CO}–O_{CO}. (f) DFT + U charge density difference ($\Delta\rho$) for the $(Ni_{10}O_8$-CO)-2(PHI) system. Yellow and cyan colors are used to represent the negative and positive charge density differences, respectively, with an isosurface value of 0.01. The atoms are depicted as ball-and-stick models, with nickel in green, carbon in grey, nitrogen in blue, oxygen in red, and sodium in yellow.

configuration of $(Ni_{10}O_8)^{4+}$ is chosen so that the distances between the nickel and oxygen atoms at the edges of the simulation box are consistent with a periodic NiO cluster under periodic boundary conditions (PBCs). First, we performed a DFT + U geometry optimization of the $(Ni_{10}O_8)$-2(PHI) system (Fig. 9a, c top, and d). Then, on the optimized $(Ni_{10}O_8)$-2(PHI) system, we added a CO molecular probe in the vicinity of two nickel atoms $d(Ni_n$–$C_{CO}) \approx 2$ Å, and performed another DFT + U geometry optimization on the $(Ni_{10}O_8$-CO)-2(PHI) system (Fig. 9b, c bottom, and e). The protocol used for the DFT-based static calculations follows the Computational methods section. The CO bond elongates to 1.194 Å when the CO molecule interacts with two Ni atoms of the NiO cluster in a symmetric bridge binding (Fig. 9e). The Ni_2–C_{CO} and Ni_5–C_{CO} bond lengths are nearly equivalent, at 1.976 Å and 2.000 Å, respectively (Fig. 9e). The charge density difference analysis (Fig. 9f) shows an inverted localization of negative and a positive isosurfaces on the O_{CO} and C_{CO} atoms ($^{+}C{=}O^{-}$), respectively, compared to the free CO ($^{-}C{\equiv}O^{+}$). The CO strongly binds to two Ni atoms in a Ni–CO–Ni bridge configuration with a binding energy (ΔE_B) of approximately 1.57 eV, which is lower than that of the semi-bridge interaction observed in $(Ni_2$-CO)-2(PHI) system 1. We performed Bader charge analysis on the $(Ni_{10}O_8)$-2(PHI) and corresponding $(Ni_{10}O_8$-CO)-2(PHI) optimized structures to verify whether nickel oxide preserves a positive charge within the periodic framework.[52] As reported in Table S5, the sums of the Bader charges of nickel and oxygen atoms belonging to $(Ni_{10}O_8)^{4+}$ in the $(Ni_{10}O_8)$-2(PHI) and $(Ni_{10}O_8$-CO)-2(PHI) systems were found to be positive, +1.86 $|e|$ and +2.15 $|e|$, respectively, supporting the reliability of our periodic approach. A higher positive charge was observed for both the nickel atoms interacting with CO in the $(Ni_{10}O_8$-CO)-2(PHI) system compared to the same nickel atoms in $(Ni_{10}O_8)$-2(PHI). The sum of the Bader charges in the CO probe molecule is negative, further suggesting $Ni^{2+} \rightarrow -C{\equiv}O^{+}$ π-backdonation. Overall, these findings indicate π-backdonation from Ni atoms interacting with the CO molecular probe in a bridge configuration. Additionally, to address the possible residual presence of $Ni(OH)_2$ nanoparticles, we produced a representative $(Ni_9(OH)_{14})$-2(PHI) model, selected to have the stable hexagonal β-phase $Ni(OH)_2$ crystal structure, fitting the PHI pore volume,[54] and providing a site for CO probe interaction. On this system, we performed DFT + U simulations to understand the static properties, as reported in the SI (Fig. S16).

2.6 DFT-based molecular dynamics simulations

To further understand the CO-DRIFTS findings shown in Fig. 4 and bridge them to a molecular interpretation, DFT-MD serves as an ideal approach for analyzing the dynamical effects of CO interaction with the (Ni)-2(PHI) system, (Ni_2)-2(PHI) systems **1**, **2**, and **3**, and $(Ni_{10}O_8)$-2(PHI) system as well as for following the structural rearrangements of PHI at room temperature.

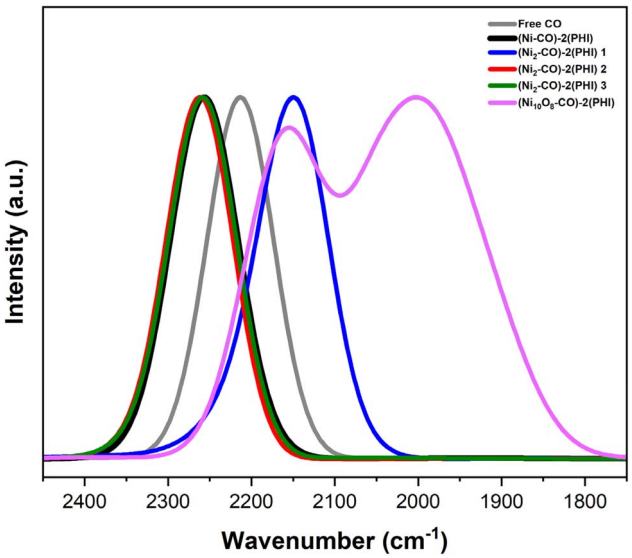

Fig. 10 Computational CO-VDOS analysis, with intensity in arbitrary units (a.u.) and frequencies (in cm^{-1}). The computational CO-VDOS are extracted from the CO molecular probe distance in the last 1.0 ps of each separate NVT DFT-MD for the free CO molecular probe, (Ni-CO)-2(PHI) system, (Ni_2-CO)-2(PHI) systems **1**, **2**, and **3**, and ($Ni_{10}O_8$-CO)-2(PHI) in grey, black, blue, red, green, and pink solid lines, respectively.

Therefore, five separate 1.25 ps NVT DFT-MD simulations were performed on the previously DFT + *U* optimized geometries of isolated free CO molecular probe, (Ni-CO)-2(PHI) system, (Ni_2-CO)-2(PHI) systems **1**, **2**, and **3**, and ($Ni_{10}O_8$)-2(PHI) system (see the Computational methods for details). After an initial 0.25 ps of thermal equilibration, both the temperature and the Kohn–Sham (KS) potential energies stabilized (Fig. S17 and S18). The remaining 1.0 ps of each trajectory was used to perform vibrational density of states (VDOS) analysis of the time evolution of the CO bond length stretching (Fig. S19), from which the frequency trends were compared with the experimental CO-DRIFTS spectra.[55] A Gaussian window function with a sigma value of 15 was chosen for each VDOS analysis. The CO stretching frequencies obtained from VDOS, named CO-VDOS, are systematically shifted by ≈ 70–80 cm^{-1} to higher values compared with the experimental CO-DRIFTS spectra. This baseline shift is inherent to the PBE0-D3 functional, which typically overestimates CO stretching frequencies (Table S3).[56] Nevertheless, PBE0-D3 reduces delocalization error compared with GGA functionals, such as PBE, providing insightful results.[57] The CO-VDOS analysis serves as a guide to understand the trend in the CO stretching frequencies observed in the CO-DRIFTS results and to interpret them at the molecular level, rather than to provide simulated CO frequencies for direct comparison with the CO-DRIFTS ones. We analyzed the CO-VDOS of free CO, which peaks at 2213 cm^{-1} (Fig. 10 grey line), consistent with the ≈ 70 cm^{-1} PBE0 shift with respect to the experimental gas-phase frequency of 2143 cm^{-1}.[56] The (Ni-CO)-2(PHI) system, and the (Ni_2-CO)-2(PHI) systems **2** and **3** exhibit CO-VDOS blue-shifted to higher frequencies around 2260 cm^{-1} (Fig. 10 black, red, and green lines) compared to free CO, indicating that the CO bond remains strongly polarized, oscillating at shorter values than free CO (Fig. S19). These CO-VDOS frequencies, after accounting for the systematic PBE0 overestimation of ≈70–80 cm^{-1}, agree well with the CO-DRIFTS peaks at 2190 cm^{-1} for low nickel concentrations (0.5 wt% and 1 wt%), as shown in Fig. 4, where a Ni–CO linear σ-bond interaction is suggested. In contrast, the CO-VDOS for (Ni_2-CO)-2(PHI) system **1** is red-shifted compared to free CO (Fig. 10 blue line). This CO-VDOS frequency, ranging around 2150 cm^{-1}, shows close agreement with the CO-DRIFTS results in the range of 2000–2080 cm^{-1} for high nickel loadings (2 wt% and 4 wt%) displayed in Fig. 4, once the intrinsic PBE0 frequency shift (≈70–80 cm^{-1}) is taken into account. The CO bond length fluctuates to larger values than free CO (Fig. S19), pointing out a less polarized bond in line with the shift to lower frequencies. Interestingly, during the DFT-MD of (Ni_2-CO)-2(PHI) system **1**, the PHI layers exhibited a larger stacking shift relative to the (Ni)-2(PHI) system, and (Ni_2-CO)-2(PHI) systems **2** and **3** (Fig. S20). This stacking movement in (Ni_2-CO)-2(PHI) system **1** at 1.25 ps introduces a third nitrogen atom from the PHI framework into interaction with Ni^{2+} positioned farthest from the CO (Fig. S21b), thereby stabilizing the configuration energetically compared to systems **2** and **3** (Fig. S18). In this arrangement, the CO bond length in (Ni_2-CO)-2(PHI) system **1** continues to oscillate at larger values compared to the (Ni)-2(PHI) system, and (Ni_2-CO)-2(PHI) systems **2** and **3** (Fig. S19). For system **1**, the semi-bridge Ni–CO–Ni bond lengths fluctuate during the DFT-MD trajectory from 2.01 Å and 3.88 Å at 0.25 ps, 1.86 Å and 3.14 Å at 0.5 ps, 1.94 Å and 2.44 Å at 0.75 ps, 1.86 Å and 3.94 Å at 1.0 ps, and 1.87 Å and 3.53 Å at 1.25 ps (Fig S21b and S22). In the NiO-nanoparticle representative model with the CO molecular probe, ($Ni_{10}O_8$-CO)-2(PHI), the CO-VDOS results in a broad and bimodal curve with two peaks around 2150 cm^{-1} and 2000 cm^{-1} (Fig. 10 pink line), respectively, red-shifted with respect to free CO. This broad CO-VDOS, considering the PBE0-based offset of ≈70–80 cm^{-1}, is found to be in agreement with the CO-DRIFTS ones within the range of 2080–2000 cm^{-1} at high nickel loading (2 wt% and 4 wt%) reported in Fig. 4. This CO-VDOS behaviour arises from the dynamic movement of the CO molecular probe, changing the type of interactions on the NiO-nanoparticle surface, from a Ni–CO–Ni bridge to a semi-bridge configuration (Fig. S21 and S22). The Ni–CO–Ni bond lengths oscillate during the DFT-MD trajectory from 2.01 Å and 2.12 Å at 0.25 ps, 2.00 Å and 2.01 Å at 0.5 ps, 2.00 Å and 2.39 Å at 0.75 ps, 1.77 Å and 3.96 Å at 1.0 ps, and 1.71 Å and 3.82 Å at 1.25 ps (Fig. S21 and S22). The presence of NiO-nanoparticles can provide stable Ni–CO–Ni interactions, alternating between a bridge and a semi-bridge type, while in both cases the $Ni^{2+} \rightarrow -C{\equiv}O^{+}$ π-backdonation is likely retained with different magnitudes. The employment of DFT-MD simulations offers valuable insight into the dynamic interactions of Ni^{2+} and NiO within the PHI layers and with the CO molecular probe at room temperature, where thermal fluctuations play a decisive role in sampling different stable configurations along the potential energy surface.

3 Conclusions

In this study, we effectively integrated experimental and multiscale computational investigations to resolve the structure of the Ni-based poly(heptazine imide) crystalline carbon nitride (Ni-PHI). The CO-DRIFTS measurements reveal that, at low nickel loadings (0.5–1 wt%), CO preferentially binds linearly to isolated Ni^{2+} single sites, whereas increasing nickel content (2–4 wt%) promotes the formation of nickel aggregates such as $Ni(OH)_2$/NiO nanoparticles, leading to the emergence of bridge-bonded Ni-CO-Ni species and a progressive red shift of the CO-DRIFTS stretching frequencies. DFT-based static and DFT-MD simulations consistently reproduce the CO-DRIFTS spectroscopic trends *via* CO-VDOS frequency analysis and provide a molecular-level understanding of the evolution of CO bonding. The simulations demonstrate that increased nickel aggregation enhances π-backdonation from Ni to CO, weakening the C–O bond and stabilizing bridge and semi-bridge Ni–CO–Ni interaction-like configurations. Thermal fluctuations captured by DFT-MD further highlight the dynamic nature of Ni coordination and PHI layer rearrangements at room temperature. Notably, recent research on M-PHI has reported enhanced catalytic activity arising from the synergy between single-atom centers and nanoparticles.[58,59] Overall, this combined experimental–computational approach establishes a coherent structural picture linking nickel loading to the transition from isolated Ni^{2+} single-atom sites to nanoparticle-like catalytic environments in Ni-PHI. This work provides important molecular insight into the catalytic site structure of Ni-PHI and introduces a transferable experimental–computational strategy for investigating the catalytic sites in various M-PHIs, thereby supporting the rational design of M-PHIs for surface and single-atom catalysis.

4 Experimental and computational methods

4.1 Experimental methods: Ni-PHI synthesis

PHI was prepared by ball-milling 1 g of melamine with 10 g of NaCl, followed by thermal treatment at 600 °C for 4 hours under a nitrogen flow (5 L min^{-1}) with a heating rate of 2.3 °C min^{-1}. After cooling, the material was washed with deionized water to remove residual salt. Cation exchange was conducted by dispersing PHI in aqueous nickel solutions at varying concentrations. The suspension was subjected to ultrasonic treatment for 30 minutes, followed by centrifugation to separate the solid. The recovered material was then dried at 80 °C overnight.

4.2 Experimental methods: Ni-PHI characterization: X-ray diffraction (XRD)

The Na-PHI precursor and the Ni-PHI materials were characterized by X-ray powder diffraction (XRD) using a Bruker D8 Advance diffractometer equipped with a Cu Kα radiation source ($\lambda = 1.5418$ Å).

4.3 Experimental methods: Ni-PHI characterization: high-angle annular dark-field scanning transmission electron microscopy (HAADF-STEM) imaging

HAADF-STEM images were acquired using a Thermo Fisher Scientific Titan Cubed Themis (TEM-Titan) equipped with a cold-field emission gun and double Cs aberration correction, operated at 300 kV, with a probe convergence semi-angle of 25 mrad. For sample preparation, the catalyst was suspended in 2-propanol, dispersed using ultrasonication for 10 min, and then deposited onto a Cu holey carbon TEM grid.

4.4 Experimental methods: CO adsorption probing *via* diffuse reflectance infrared Fourier transform spectroscopy (CO-DRIFTS)

The CO-DRIFTS analysis was performed using a Nicolet iS50 FTIR spectrometer equipped with a Praying Mantis accessory and a Harrick reaction cell. The sample was pretreated at 300 °C under a He flow (20 mL min^{-1}) for 10 min. After cooling to room temperature, a reference spectrum (baseline) was recorded under He prior to CO exposure. CO was then introduced for 10 min (with the He flow temporarily stopped), followed by a He purge for 15 min to remove physisorbed species, after which a post-desorption spectrum was collected. All spectra presented in this work correspond to difference spectra (ΔDRIFTS), obtained by subtracting the baseline spectrum from the post-desorption spectrum (Fig. S23). This baseline subtraction allows isolating the vibrational features specifically associated with CO adsorption and its interaction with Ni sites. Spectra were recorded with a resolution of 1 cm^{-1} and averaged over 256 scans.

4.5 Computational methods: DFT and DFT + U static simulations

Spin-polarized DFT and DFT + *U* calculations were carried out by using the Vienna *Ab initio* Simulation Package (VASP).[60] The projector-augmented wave (PAW) pseudopotential and the Perdew–Burke–Ernzerhof (PBE) exchange-correlation functional within the generalized gradient approximation (GGA) were considered to describe the interactions between valence electrons and ionic cores and the exchange-correlation effects, respectively.[61,62] The kinetic cutoff energy was set to 400 eV for the wave function calculations. The lattice parameters *a*, *b*, and *c*, and α, β, and γ of the simulation cell are 26.081 Å, 26.081 Å, and 8.504 Å, and 98.1°, 112.1°, and 119.8°, respectively, as represented in Fig. S6. A vacuum gap of ~1.80 Å was chosen to account for interactions between the system and its mirror images, based on the crystal structure.[20] The bulk model takes into consideration the multilayered disorder nature of the PHI framework,[63] also during the CO molecular probe interaction. The van der Waals interaction was described using the Grimme *et al.* D3 dispersion correction.[64] The convergence criteria were set to be 1×10^{-5} eV for energy change and 0.05 eV $Å^{-1}$ for force change during the geometrical optimization. To accurately describe and compare the Ni properties, we performed DFT + *U* calculations. The Hubbard correction was applied to the Ni

element, with a U-value of 3.40 eV, in agreement with the previous literature and benchmarks.[27,45,46] The charge density difference analysis was performed using the VASPKIT code.[65] The benchmark of the periodic system calculations with total net charge zero was carried out using molecular complexes such as $[Ni\text{-}(melem)_2)]^{2+}$ and $[(Ni\text{-}CO)\text{-}(melem)_2)]^{2+}$ through spin-polarized (unrestricted) DFT calculations with the Gaussian 16 code.[66] We employed the PBE0-D3 hybrid functional,[67,68] for the optimization and frequency calculations, using the 6−31++G(d, p) basis set with diffuse functions for all atoms.[69,70] For the (Ni_{1or2}-CO)-2(PHI) geometry optimizations, the CO molecular probe was placed in proximity to each nickel atom, at a Ni_{1or2}–C_{CO} distance $d(Ni_{1or2}\text{–}C_{CO}) \approx 2$ Å, and in two positions with respect to the nickel atoms, along the x–y and z planes, respectively (Fig. S8). On these structures, we performed DFT and DFT + U geometry optimizations at the GGA level described above. Successively, the Ni–CO binding energies (ΔE_B) were estimated for each Ni_{1or2} and NiO-nanoparticle system (Ni_{system}) as the difference, $\Delta E_B = E_{(Nisystem\text{-}CO)\text{-}2(PHI)} - E_{Nisystem\text{-}2(PHI)} - E_{CO}$, performing for each optimized (Ni_{system}-CO)-2(PHI) system separate single-point calculations on (Ni_{system}-CO)-2(PHI), and its components Ni_{system}-2(PHI) and CO, respectively.

4.6 Computational methods: DFT-based molecular dynamics simulations

The spin-polarized (unrestricted) DFT-MD NVT simulations were carried out using periodic boundary conditions (PBCs) and the hybrid Gaussian and plane wave approach,[71] as implemented in the CP2K/Quickstep code.[72] The spin multiplicity employed is singlet for the (Ni)-2(PHI) system, and quintet for (Ni_2-CO)-2(PHI) systems **1**, **2**, and **3**, and also for the ($Ni_{10}O_8$)-2(PHI) system, noting that for the latter the multiplicity is an imposed constraint to maintain consistency with the two-Ni reference systems, since at room temperature a small NiO-nanoparticle surface is likely highly paramagnetic.[73] The Kohn–Sham (KS) orbitals were described by an accurate molecularly optimized double-zeta basis set with one additional set of polarization functions (DZVP-MOLOPT-GTH), while the charge density was represented by plane waves with a density cutoff of 600 Ry.[74] Separable norm-conserving pseudopotentials were used to mimic the interactions between the valence electrons and the ionic cores.[75,76] The PBE0 hybrid functional was employed because it has been shown to be highly accurate in describing transition-metal complexes and is suggested for describing CO vibrations when CO interacts with Ni^{2+} ion(s).[27,67,68] The damped D3 atom-pairwise Grimme dispersion correction was added to account for long-range van der Waals interactions.[64] A Nosé-Hoover chain (NHC) thermostat was used, with a chain length and thermostat time constant of 7 and 10 fs, respectively, and the time step and temperature were 0.5 fs and 300 K, respectively.

Author contributions

D. C., I. F. T., A. K., and T. D. K. conceived the idea to computationally and experimentally study the Ni-PHI catalytic site structures. D. C. performed the DFT-based static and MD simulations and analyzed and interpreted all the simulations. D. C. coordinated the project. D. C. wrote the manuscript with the help of all authors. I. G. F. and D. N. B. performed the synthesis, XRD and EDS characterization, and CO-DRIFTS analysis. L. F. G. N. collected and analyzed the HAADF-STEM data. M. A. R. d. S. performed and interpreted the XPS characterization. T. D. K. and A. K. supervised the computational work. I. F. T. supervised the experimental work.

Conflicts of interest

There are no conflicts to declare.

Data availability

The computational metadata, including DFT-based static and DFT-MD data, and the plots' raw data are provided as the supplementary information (SI), openly available in the ZENODO EU Open Research Repository at https://doi.org/10.5281/zenodo.19814862. All the remaining data will be available upon a reasonable request.

Supplementary information: characterization of Ni-PHI; S2. Computational results on Ni_{1or2}-2(PHI) and (Ni_{1or2}-CO)-2(PHI): DFT-based static simulations; S3. Computational results on a NiO/$Ni(OH)_2$-nanoparticle representative models: DFT-based static simulations; S4. Computational results: DFT-based molecular dynamics simulations. See DOI: https://doi.org/10.1039/d6ta01987k.

Acknowledgements

We acknowledge the computing time provided on the high-performance computers Beaker and Noctua 2 at the NHR Centers NHR@TUD (ZIH) and NHR@Padeborn (PC2). A. K. and T. D. K. acknowledge the Deutsche Forschungsgemeinschaft (DFG) within the CRC 1415 project. A. K. acknowledges Dr Jan-Ole Joswig for the fruitful discussions. I. F. T. acknowledges that the experimental research was financially supported by the Brazilian funding agencies CAPES, CNPq (403064/2021 and 405752/2022), FAPESP (2020/14741-6, 2021/11162-8, 2024/00839-5, 2021/12394-0, and 2021/13271-9), and FINEP (01.23.0645.00 and 01.23.0662.00). L. F. G. N. and I.G.F. are grateful to FAPESP for their scholarships (2022/14652-9 and 2022/13249-6). Dr Carlos Ospina Ramirez and LNNano are greatly acknowledged for their support with STEM data collection (TEM-20210344 and TEM-C1-20232675).

References

1 G. F. S. R. Rocha, M. A. R. Da Silva, A. Rogolino, G. A. A. Diab, L. F. G. Noleto, M. Antonietti and I. F. Teixeira, Carbon Nitride Based Materials: More than Just a Support for Single-Atom Catalysis, *Chem. Soc. Rev.*, 2023, **52**(15), 4878–4932, DOI: 10.1039/D2CS00806H.

2 M. Zhou, H. Ou, Z. Liu, Z. Jiang, C. Yang, Y. Fang, S. Wang, G. Zhang, J. Cheng, Y. Hou and X. Wang, Poly(Heptazine

Imide): Crystalline Allotrope of Polymeric Carbon Nitrides for Solar to Chemical Energy Conversion, *Angew. Chem., Int. Ed.*, 2026, **65**(14), e1708637, DOI: 10.1002/anie.1708637.

3 C. M. Pelicano and M. Antonietti, Metal Poly(Heptazine Imides) as Multifunctional Photocatalysts for Solar Fuel Production, *Angew. Chem., Int. Ed.*, 2024, **63**(24), e202406290, DOI: 10.1002/anie.202406290.

4 S. Cao, J. Low, J. Yu and M. Jaroniec, Polymeric Photocatalysts Based on Graphitic Carbon Nitride, *Adv. Mater.*, 2015, **27**(13), 2150–2176, DOI: 10.1002/adma.201500033.

5 D. Dontsova, S. Pronkin, M. Wehle, Z. Chen, C. Fettkenhauer, G. Clavel and M. Antonietti, Triazoles: A New Class of Precursors for the Synthesis of Negatively Charged Carbon Nitride Derivatives, *Chem. Mater.*, 2015, **27**(15), 5170–5179, DOI: 10.1021/acs.chemmater.5b00812.

6 Savateev, A., Antonietti, M., & Wang, X. ed. *Carbon Nitrides: Structure, Properties and Applications in Science and Technology*, Berlin, Boston: De Gruyter. 2023, DOI: 10.1515/9783110746976. https://Hdl.Handle.Net/21.11116/0000-000D-4D29-0.

7 H. Schlomberg, J. Kröger, G. Savasci, M. W. Terban, S. Bette, I. Moudrakovski, V. Duppel, F. Podjaski, R. Siegel, J. Senker, R. E. Dinnebier, C. Ochsenfeld and B. V. Lotsch, Structural Insights into Poly(Heptazine Imides): A Light-Storing Carbon Nitride Material for Dark Photocatalysis, *Chem. Mater.*, 2019, **31**(18), 7478–7486, DOI: 10.1021/acs.chemmater.9b02199.

8 A. Savateev, S. Pronkin, M. G. Willinger, M. Antonietti and D. Dontsova, Towards Organic Zeolites and Inclusion Catalysts: Heptazine Imide Salts Can Exchange Metal Cations in the Solid State, *Chem. Asian J.*, 2017, **12**(13), 1517–1522, DOI: 10.1002/asia.201700209.

9 J. Kröger, F. Podjaski, G. Savasci, I. Moudrakovski, A. Jiménez-Solano, M. W. Terban, S. Bette, V. Duppel, M. Joos, A. Senocrate, R. Dinnebier, C. Ochsenfeld and B. V. Lotsch, Conductivity Mechanism in Ionic 2D Carbon Nitrides: From Hydrated Ion Motion to Enhanced Photocatalysis, *Adv. Mater.*, 2022, **34**(7), 2107061, DOI: 10.1002/adma.202107061.

10 S. K. Sahoo, I. F. Teixeira, A. Naik, J. Heske, D. Cruz, M. Antonietti, A. Savateev and T. D. Kühne, Photocatalytic Water Splitting Reaction Catalyzed by Ion-Exchanged Salts of Potassium Poly(Heptazine Imide) 2D Materials, *J. Phys. Chem. C*, 2021, **125**(25), 13749–13758, DOI: 10.1021/acs.jpcc.1c03947.

11 M. A. R. Da Silva, J. C. Gil, N. V. Tarakina, G. T. S. T. Silva, J. B. G. Filho, K. Krambrock, M. Antonietti, C. Ribeiro and I. F. Teixeira, Selective Methane Photooxidation into Methanol under Mild Conditions Promoted by Highly Dispersed Cu Atoms on Crystalline Carbon Nitrides, *Chem. Commun.*, 2022, **58**(53), 7419–7422, DOI: 10.1039/D2CC01757A.

12 G. A. A. Diab, I. F. Reis, C. Wang, D. Barreto, O. Savateev, I. F. Teixeira and P. Jiménez-Calvo, Ionic Metal Poly(Heptazine Imides) and Single-Atoms Interplay: Engineered Stability and Performance for Photocatalysis, Photoelectrocatalysis and Organic Synthesis, *Adv. Funct. Mater.*, 2025, 2501393, DOI: 10.1002/adfm.202501393.

13 Z. Hajiahmadi, A. Lo Presti, S. S. Naghavi, M. Antonietti, C. M. Pelicano and T. D. Kühne, Theory-Guided Discovery of Ion-Exchanged Poly(Heptazine Imide) Photocatalysts Using First-Principles Many-Body Perturbation Theory, *J. Am. Chem. Soc.*, 2026, **148**(2), 2165–2174, DOI: 10.1021/jacs.5c09930.

14 X. Liang, S. Xue, M. Shen, Y. Ye, H. Zhuzhang, W. Xing, C. Yang, Z. Yu, G. Zhang and X. Wang, Unraveling the Correlation between Crystallographic Structure and Charge Transport in Metal Poly(Heptazine Imides), *J. Am. Chem. Soc.*, 2025, **147**(49), 45712–45722, DOI: 10.1021/jacs.5c17982.

15 Y. Jin, D. Zheng, Z. Fang, Z. Pan, S. Wang, Y. Hou, O. Savateev, Y. Zhang and G. Zhang, Salt-melt Synthesis of Poly(Heptazine Imide) in Binary Alkali Metal Bromides for Enhanced Visible-light Photocatalytic Hydrogen Production, *Interdiscip. Mater.*, 2024, **3**(3), 389–399, DOI: 10.1002/idm2.12159.

16 Y. Zou, H. Chen, Y. Hou, W. Xing, Z. Pan, O. Savateev, M. Anpo and G. Zhang, Efficient Photocatalytic Hydrogen Production Coupled with Glycerol Valorization Driven by Fully Condensed Potassium Poly (Heptazine Imides), *Adv. Funct. Mater.*, 2026, **36**(6), e16479, DOI: 10.1002/adfm.202516479.

17 Z. Hu, Z. Yang, S. Zeng, K. Wang, L. Li, C. Hu and Y. Zhao, Cationic Surface Polarization Centers on Ionic Carbon Nitride for Efficient Solar-Driven H2O2 Production and Pollutant Abatement, *Chin. Chem. Lett.*, 2024, **35**(10), 109526, DOI: 10.1016/j.cclet.2024.109526.

18 X. Li, W. Bi, L. Zhang, S. Tao, W. Chu, Q. Zhang, Y. Luo, C. Wu and Y. Xie, Single-Atom Pt as Co-Catalyst for Enhanced Photocatalytic H_2 Evolution, *Adv. Mater.*, 2016, **28**(12), 2427–2431, DOI: 10.1002/adma.201505281.

19 Z. Chen, E. Vorobyeva, S. Mitchell, E. Fako, N. López, S. M. Collins, R. K. Leary, P. A. Midgley, R. Hauert and J. Pérez-Ramírez, Single-Atom Heterogeneous Catalysts Based on Distinct Carbon Nitride Scaffolds, *Natl. Sci. Rev.*, 2018, **5**(5), 642–652, DOI: 10.1093/nsr/nwy048.

20 M. A. R. Da Silva, I. F. Silva, Q. Xue, B. T. W. Lo, N. V. Tarakina, B. N. Nunes, P. Adler, S. K. Sahoo, D. W. Bahnemann, N. López-Salas, A. Savateev, C. Ribeiro, T. D. Kühne, M. Antonietti and I. F. Teixeira, Sustainable Oxidation Catalysis Supported by Light: Fe-Poly (Heptazine Imide) as a Heterogeneous Single-Atom Photocatalyst, *Appl. Catal. B Environ.*, 2022, **304**, 120965, DOI: 10.1016/j.apcatb.2021.120965.

21 F. M. Colombari, M. A. R. Da Silva, M. S. Homsi, B. R. L. De Souza, M. Araujo, J. L. Francisco, G. T. S. T. Da Silva, I. F. Silva, A. F. De Moura and I. F. Teixeira, Graphitic Carbon Nitrides as Platforms for Single-Atom Photocatalysis, *Faraday Discuss.*, 2021, **227**, 306–320, DOI: 10.1039/C9FD00112C.

22 A. Rogolino, I. F. Silva, N. V. Tarakina, M. A. R. Da Silva, G. F. S. R. Rocha, M. Antonietti and I. F. Teixeira, Modified Poly(Heptazine Imides): Minimizing H_2O_2 Decomposition to Maximize Oxygen Reduction, *ACS Appl.*

Mater. Interfaces, 2022, **14**(44), 49820–49829, DOI: 10.1021/acsami.2c14872.

23 M. A. R. Da Silva, G. F. S. R. Rocha, G. A. A. Diab, C. S. Cunha, V. G. S. Pastana and I. F. Teixeira, Simple and Straightforward Method to Prepare Highly Dispersed Ni Sites for Selective Nitrobenzene Coupling to Azo/Azoxy Compounds, *Chem. Eng. J.*, 2023, **460**, 141068, DOI: 10.1016/j.cej.2022.141068.

24 S. F. Blaskievicz, I. F. Teixeira, L. H. Mascaro, M. Carta, N. B. McKeown, Y. Zhao and F. Marken, Hydrogen-Mediated Photoelectrocatalysis with Nickel-Modified Poly(Heptazine Imides), *Electrocatalysis*, 2024, **15**(1), 42–51, DOI: 10.1007/s12678-023-00852-9.

25 J. B. G. Filho, L. F. G. Noleto, G. D. Iga, F. S. Gonçalves, D. R. Cardoso, I. F. Teixeira and C. Ribeiro, Visible Light-Driven Selective C C Cleavage of Glycerol into Formic Acid Using Ni-Poly(Heptazine) Imide, *Chem. Eng. J.*, 2025, **521**, 166306, DOI: 10.1016/j.cej.2025.166306.

26 L. F. Guimarães Noleto, M. A. Ribeiro Da Silva, V. Gabriel Da Silva Pastana, J. B. Gabriel Filho, K. Krambrock, B. T. W. Lo, S. Stolfi, P. Ghigna, M. Fagnoni, L. Braglia, D. Ravelli, P. Torelli and I. F. Teixeira, Proton Source Selective Semi-Hydrogenation of Alkynes: A Water-Powered Selective Photocatalyst Based on Nickel Single-Atoms on Poly(Heptazine Imide), *J. Mater. Chem. A*, 2026, **14**(8), 4478–4489, DOI: 10.1039/D5TA06939D.

27 N. Allasia, S. Xu, S. F. Jafri, E. Borfecchia, L. A. Cipriano, G. Terraneo, S. Tosoni, L. Mino, G. Di Liberto, G. Pacchioni and G. Vilé, Resolving the Nanostructure of Carbon Nitride-Supported Single-Atom Catalysts, *Small*, 2025, 2408286, DOI: 10.1002/smll.202408286.

28 D. V. Piankova, H. Zschiesche, A. P. Tyutyunnik, E. Svensson Grape, C. V. C. R. Da Silva, W. G. Guimarães Junior, M. De, F. Andre., I. F. Reis, G. A. A. Diab, J. B. G. Filho, I. F. Teixeira and N. V. Tarakina, Enhancing the Photocatalytic Performance of Carbon Nitrides Through Controlled Local Structure Modification, *Adv. Funct. Mater.*, 2025, e11389, DOI: 10.1002/adfm.202511389.

29 K. Bhunia, S. Khilari, M. Chandra, D. Pradhan and S.-J. Kim, Carbon Nitride Anchored NiO Nanoparticles as Robust Catalyst for Electrochemical Oxygen Evolution Reaction, *J. Alloys Compd.*, 2023, **935**, 167842, DOI: 10.1016/j.jallcom.2022.167842.

30 S. Ye and X. Guan, HMT-Controlled Synthesis of Mesoporous NiO Hierarchical Nanostructures and Their Catalytic Role towards the Thermal Decomposition of Ammonium Perchlorate, *Appl. Sci.*, 2019, **9**(13), 2599, DOI: 10.3390/app9132599.

31 M. C. Biesinger, B. P. Payne, A. P. Grosvenor, L. W. M. Lau, A. R. Gerson and R. St. C. Smart, Resolving Surface Chemical States in XPS Analysis of First Row Transition Metals, Oxides and Hydroxides: Cr, Mn, Fe, Co and Ni, *Appl. Surf. Sci.*, 2011, **257**(7), 2717–2730, DOI: 10.1016/j.apsusc.2010.10.051.

32 B. P. Payne, M. C. Biesinger and N. S. McIntyre, Use of Oxygen/Nickel Ratios in the XPS Characterisation of Oxide Phases on Nickel Metal and Nickel Alloy Surfaces, *J. Electron Spectrosc. Relat. Phenom.*, 2012, **185**(5–7), 159–166, DOI: 10.1016/j.elspec.2012.06.008.

33 H. Ou, P. Yang, L. Lin, M. Anpo and X. Wang, Carbon Nitride Aerogels for the Photoredox Conversion of Water, *Angew. Chem., Int. Ed.*, 2017, **56**(36), 10905–10910, DOI: 10.1002/anie.201705926.

34 M. Benedet, D. Barreca, G. A. Rizzi, C. Maccato, J.-L. Wree, A. Devi and A. Gasparotto, Fe2O3-Graphitic Carbon Nitride Nanocomposites Analyzed by XPS, *Surf. Sci. Spectra*, 2023, **30**(2), 024021, DOI: 10.1116/6.0002979.

35 M. Benedet, A. Gasparotto, G. A. Rizzi, C. Maccato, D. Mariotti, R. McGlynn and D. Barreca, XPS Investigation of MnO2 Deposits Functionalized with Graphitic Carbon Nitride, *Surf. Sci. Spectra*, 2023, **30**(2), 024018, DOI: 10.1116/6.0002827.

36 M. Mihaylov and K. Hadjiivanov, FTIR Study of CO and NO Adsorption and Coadsorption on Ni-ZSM-5 and Ni/SiO_2, *Langmuir*, 2002, **18**(11), 4376–4383, DOI: 10.1021/la015739g.

37 G. Martra, S. Coluccia, M. Che, L. Manceron, M. Kermarec and D. Costa, Ni and CO Used as Probes of the Amorphous Silica Surface: IR and Theoretical Studies of Dicarbonyl Ni^{II} Complexes, *J. Phys. Chem. B*, 2003, **107**(25), 6096–6104, DOI: 10.1021/jp034794q.

38 E. Kordouli, B. Pawelec, C. Kordulis, A. Lycourghiotis and J. L. G. Fierro, Hydrodeoxygenation of Phenol on Bifunctional Ni-Based Catalysts: Effects of Mo Promotion and Support, *Appl. Catal. B Environ.*, 2018, **238**, 147–160, DOI: 10.1016/j.apcatb.2018.07.012.

39 L. Kubelkova, J. Nováková, N. I. Jaeger and E. , Schulz, G. Characterization of Nickel Species at Ni/γ-Al203 and Ni/Faujasite Catalysts by Carbon Monoxide Adsorption, *Appl. Catal., A*, 1993, **95**(1), 87–101, DOI: 10.1016/0926-860X(93)80199-Z.

40 C. C. Zhang, J. Shi, S. Hartlaub, J. P. Palamara, I. Petrovic and B. Yilmaz, In-Situ Diffuse Reflective Infrared Fourier Transform Spectroscopy (DRIFTS) Study on Ni Passivation in FCC Catalysts from Boron-Based Technology, *Catal. Commun.*, 2021, **150**, 106273, DOI: 10.1016/j.catcom.2020.106273.

41 R. Martí Valls, R. García Rodríguez, D. Meza Rojas, T. Dunlop, E. Jones, S. K. Thomas, M. L. Davies, P. J. Holliman, J. Baker and C. Charbonneau, A Facile Method to Obtain Colloidal Dispersions of Nickel Hydroxide: Improving the Processing of Nickel Oxide and Facilitating Its Upscaling for Perovskite-Type Solar Devices, *Colloids Surf., A Physicochem. Eng. Asp.*, 2024, **698**, 134524, DOI: 10.1016/j.colsurfa.2024.134524.

42 D. Wang, R. Xu, X. Wang and Y. Li, NiO Nanorings and Their Unexpected Catalytic Property for CO Oxidation, *Nanotechnology*, 2006, **17**(4), 979–983, DOI: 10.1088/0957-4484/17/4/023.

43 C. Liu, J. Liu and R. Godin, ALD-Deposited NiO Approaches the Performance of Platinum as a Hydrogen Evolution Cocatalyst on Carbon Nitride, *ACS Catal.*, 2023, **13**(1), 573–586, DOI: 10.1021/acscatal.2c04795.

44 E. Scattolin, M. Benedet, D. Barreca, G. A. Rizzi, A. Gasparotto and C. Maccato, Graphitic Carbon Nitride

Functionalized with NiO Nanoaggregates: An X-Ray Photoelectron Spectroscopy Investigation, *Surf. Sci. Spectra*, 2024, **31**(2), 024001, DOI: 10.1116/6.0003732.

45 G. Di Liberto, L. A. Cipriano and G. Pacchioni, Universal Principles for the Rational Design of Single Atom Electrocatalysts? Handle with Care, *ACS Catal.*, 2022, **12**(10), 5846–5856, DOI: 10.1021/acscatal.2c01011.

46 I. V. Solovyev, P. H. Dederichs and V. I. Anisimov, Corrected Atomic Limit in the Local-Density Approximation and the Electronic Structure of *d* Impurities in Rb, *Phys. Rev. B*, 1994, **50**(23), 16861–16871, DOI: 10.1103/PhysRevB.50.16861.

47 X. Zhang, H. Su, P. Cui, Y. Cao, Z. Teng, Q. Zhang, Y. Wang, Y. Feng, R. Feng, J. Hou, X. Zhou, P. Ma, H. Hu, K. Wang, C. Wang, L. Gan, Y. Zhao, Q. Liu, T. Zhang and K. Zheng, Developing Ni Single-Atom Sites in Carbon Nitride for Efficient Photocatalytic H2O2 Production, *Nat. Commun.*, 2023, **14**(1), 7115, DOI: 10.1038/s41467-023-42887-y.

48 G. Frenking, C. Loschen, A. Krapp, S. Fau and S. H. Strauss, Electronic Structure of CO—An Exercise in Modern Chemical Bonding Theory, *J. Comput. Chem.*, 2007, **28**(1), 117–126, DOI: 10.1002/jcc.20477.

49 A. J. Lupinetti, S. H. Strauss, G. Frenking, Nonclassical Metal Carbonyls, In *Progress in Inorganic Chemistry*, John Wiley & Sons, Ltd, 2001, pp 1–112, DOI: 10.1002/9780470166512.ch1.

50 P. G. Lustemberg, P. N. Plessow, Y. Wang, C. Yang, A. Nefedov, F. Studt, C. Wöll and M. V. Ganduglia-Pirovano, Vibrational Frequencies of Cerium-Oxide-Bound CO: A Challenge for Conventional DFT Methods, *Phys. Rev. Lett.*, 2020, **125**(25), 256101, DOI: 10.1103/PhysRevLett.125.256101.

51 G. Bistoni, S. Rampino, N. Scafuri, G. Ciancaleoni, D. Zuccaccia, L. Belpassi and F. Tarantelli, How π Back-Donation Quantitatively Controls the CO Stretching Response in Classical and Non-Classical Metal Carbonyl Complexes, *Chem. Sci.*, 2016, **7**(2), 1174–1184, DOI: 10.1039/C5SC02971F.

52 W. Tang, E. Sanville and G. Henkelman, A Grid-Based Bader Analysis Algorithm without Lattice Bias, *J. Phys.: Condens. Matter*, 2009, **21**(8), 084204, DOI: 10.1088/0953-8984/21/8/084204.

53 H. F. Etefa, F. T. Geldasa and F. B. Dejene, Band Structure and Optical Characteristics of P-Type NiO Nanoparticles: Insights from Experiment and Density Functional Theory (DFT), *Opt. Quant. Electron.*, 2025, **57**(11), 607, DOI: 10.1007/s11082-025-08523-3.

54 A. J. Tkalych, K. Yu and E. A. Carter, Structural and Electronic Features of β-Ni(OH)$_2$ and β-NiOOH from First Principles, *J. Phys. Chem. C*, 2015, **119**(43), 24315–24322, DOI: 10.1021/acs.jpcc.5b08481.

55 D. Calvani, R. Louwersheimer and F. Buda, Effect of Anchoring Dynamics on Proton-Coupled Electron Transfer in the Ru(Bda) Coordination Oligomer on a Graphitic Surface, *ChemPlusChem*, 2024, e202400082, DOI: 10.1002/cplu.202400082.

56 H.-Z. Ye and T. C. Berkelbach, Adsorption and Vibrational Spectroscopy of CO on the Surface of MgO from Periodic Local Coupled-Cluster Theory, *Faraday Discuss.*, 2024, **254**, 628–640, DOI: 10.1039/D4FD00041B.

57 N. Mardirossian and M. Head-Gordon, Thirty Years of Density Functional Theory in Computational Chemistry: An Overview and Extensive Assessment of 200 Density Functionals, *Mol. Phys.*, 2017, **115**(19), 2315–2372, DOI: 10.1080/00268976.2017.1333644.

58 B. Su, S. Wang, W. Xing, K. Liu, S. Hung, X. Chen, Y. Fang, G. Zhang, H. Zhang and X. Wang, Synergistic Ru Species on Poly(Heptazine Imide) Enabling Efficient Photocatalytic CO_2 Reduction with H_2 O beyond 800 Nm, *Angew. Chem., Int. Ed.*, 2025, **64**(27), e202505453, DOI: 10.1002/anie.202505453.

59 X. Xu, B. Su, S. Wang, W. Xing, S. Hung, Z. Pan, Y. Fang, G. Zhang, H. Zhang and X. Wang, CO_2 Photoreduction by H_2 O: Cooperative Catalysis of Palladium Species on Poly(Triazine Imide) Crystals, *Angew. Chem., Int. Ed.*, 2025, **64**(39), e202512386, DOI: 10.1002/anie.202512386.

60 G. Kresse and J. Furthmüller, Efficient Iterative Schemes for *Ab Initio* Total-Energy Calculations Using a Plane-Wave Basis Set, *Phys. Rev. B*, 1996, **54**(16), 11169–11186, DOI: 10.1103/PhysRevB.54.11169.

61 P. E. Blöchl, Projector Augmented-Wave Method, *Phys. Rev. B*, 1994, **50**(24), 17953–17979, DOI: 10.1103/PhysRevB.50.17953.

62 J. P. Perdew, K. Burke and M. Ernzerhof, Generalized Gradient Approximation Made Simple, *Phys. Rev. Lett.*, 1996, **77**(18), 3865–3868, DOI: 10.1103/PhysRevLett.77.3865.

63 D. Khaykelson, G. A. A. Diab, S. R. Cohen, T. Kashti, T. Bendikov, I. Pinkas, I. F. Teixeira, N. V. Tarakina, L. Houben and B. Rybtchinski, Elucidating Structural Disorder in a Polymeric Layered Material: The Case of Sodium Poly(Heptazine Imide) Photocatalyst, *Nano Lett.*, 2025, **25**(49), 17230–17236, DOI: 10.1021/acs.nanolett.5c04946.

64 S. Grimme, J. Antony, S. Ehrlich and H. Krieg, A Consistent and Accurate *Ab Initio* Parametrization of Density Functional Dispersion Correction (DFT-D) for the 94 Elements H-Pu, *J. Chem. Phys.*, 2010, **132**(15), 154104, DOI: 10.1063/1.3382344.

65 V. Wang, N. Xu, J.-C. Liu, G. Tang and W.-T. Geng, VASPKIT: A User-Friendly Interface Facilitating High-Throughput Computing and Analysis Using VASP Code, *Comput. Phys. Commun.*, 2021, **267**, 108033, DOI: 10.1016/j.cpc.2021.108033.

66 M. J. Frisch, G. W. Trucks, H. B. Schlegel, G. E. Scuseria, M. A. Robb, J. R. Cheeseman, G. Scalmani, V. Barone, G. A. Petersson, H. Nakatsuji, X. Li, M. Caricato, A. V. Marenich, J. Bloino, B. G. Janesko, R. Gomperts, B. Mennucci, H. P. Hratchian, J. V. Ortiz, A. F. Izmaylov, J. L. Sonnenberg, D. Williams-Young, F. Ding, F. Lipparini, F. Egidi, J. Goings, B. Peng, A. Petrone, T. Henderson, D. Ranasinghe, V. G. Zakrzewski, J. Gao, N. Rega, G. Zheng, W. Liang, M. Hada, M. Ehara, K. Toyota, R. Fukuda, J. Hasegawa, M. Ishida, T. Nakajima, Y. Honda, O. Kitao, H. Nakai, T. Vreven, K. Throssell, J. A. Montgomery Jr., J. E. Peralta, F. Ogliaro, M. J. Bearpark, J. J. Heyd, E. N. Brothers, K. N. Kudin,

V. N. Staroverov, T. A. Keith, R. Kobayashi, J. Normand, K. Raghavachari, A. P. Rendell, J. C. Burant, S. S. Iyengar, J. Tomasi, M. Cossi, J. M. Millam, M. Klene, C. Adamo, R. Cammi, J. W. Ochterski, R. L. Martin, K. Morokuma, O. Farkas, J. B. Foresman, and D. J. Fox, Gaussian 16, Revision C.01, Gaussian, Inc., Wallingford CT, 2016.

67 C. Adamo and V. Barone, Toward Reliable Density Functional Methods without Adjustable Parameters: The PBE0 Model, *J. Chem. Phys.*, 1999, **110**(13), 6158–6170, DOI: 10.1063/1.478522.

68 M. Ernzerhof and G. E. Scuseria, Assessment of the Perdew–Burke–Ernzerhof Exchange-Correlation Functional, *J. Chem. Phys.*, 1999, **110**(11), 5029–5036, DOI: 10.1063/1.478401.

69 W. J. Hehre, R. Ditchfield and J. A. Pople, Self—Consistent Molecular Orbital Methods. XII. Further Extensions of Gaussian—Type Basis Sets for Use in Molecular Orbital Studies of Organic Molecules, *J. Chem. Phys.*, 1972, **56**(5), 2257–2261, DOI: 10.1063/1.1677527.

70 V. A. Rassolov, M. A. Ratner, J. A. Pople, P. C. Redfern and L. A. Curtiss, 6-31G* Basis Set for Third-row Atoms, *J. Comput. Chem.*, 2001, **22**(9), 976–984, DOI: 10.1002/jcc.1058.

71 G. Lippert, J. Hutter and M. Parrinello, A Hybrid Gaussian and Plane Wave Density Functional Scheme, *Mol. Phys.*, 1997, **92**(3), 477–487, DOI: 10.1080/00268979709482119.

72 T. D. Kühne, M. Iannuzzi, M. Del Ben, V. V. Rybkin, P. Seewald, F. Stein, T. Laino, R. Z. Khaliullin, O. Schütt, F. Schiffmann, D. Golze, J. Wilhelm, S. Chulkov, M. H. Bani-Hashemian, V. Weber, U. Borštnik, M. Taillefumier, A. S. Jakobovits, A. Lazzaro, H. Pabst, T. Müller, R. Schade, M. Guidon, S. Andermatt, N. Holmberg, G. K. Schenter, A. Hehn, A. Bussy, F. Belleflamme, G. Tabacchi, A. Glöß, M. Lass, I. Bethune, C. J. Mundy, C. Plessl, M. Watkins, J. VandeVondele, M. Krack and J. Hutter, CP2K: An Electronic Structure and Molecular Dynamics Software Package - Quickstep: Efficient and Accurate Electronic Structure Calculations, *J. Chem. Phys.*, 2020, **152**(19), 194103, DOI: 10.1063/5.0007045.

73 M. Tadic, D. Nikolic, M. Panjan and G. R. Blake, Magnetic Properties of NiO (Nickel Oxide) Nanoparticles: Blocking Temperature and Neel Temperature, *J. Alloys Compd.*, 2015, **647**, 1061–1068, DOI: 10.1016/j.jallcom.2015.06.027.

74 J. VandeVondele and J. Hutter, Gaussian Basis Sets for Accurate Calculations on Molecular Systems in Gas and Condensed Phases, *J. Chem. Phys.*, 2007, **127**(11), 114105, DOI: 10.1063/1.2770708.

75 S. Goedecker, M. Teter and J. Hutter, Separable Dual-Space Gaussian Pseudopotentials, *Phys. Rev. B*, 1996, **54**(3), 1703–1710, DOI: 10.1103/PhysRevB.54.1703.

76 M. Krack, Pseudopotentials for H to Kr Optimized for Gradient-Corrected Exchange-Correlation Functionals, *Theor. Chem. Acc.*, 2005, **114**(1–3), 145–152, DOI: 10.1007/s00214-005-0655-y.